Master Thesis

Development of Radiative Decay Counter for ultimate sensitivity of MEG Ⅱ experiment

訳

究極感度のMEG Ⅱ実験のための
輻射崩壊同定用カウンターの開発

Shota Nakaura

Supervisor: Prof.Wataru OOTANI
Department of Physics, School of Science,
The University of Tokyo

January 5, 2016

THE UNIVERSITY OF TOKYO

Abstract

In order to search for the charged lepton flavour violating decay (cLFV) $\mu^+ \to e^+\gamma$, the Mu to E Gamma (MEG) experiment started data-taking in 2008. The published result [1] is consistent with the background-only hypothesis and set upper limit on the branching ratio:

$$B(\mu^+ \to e^+\gamma) < 5.7 \times 10^{-13}$$

For achieving a better sensitivity, the MEG experiment will be upgraded to MEG II which will improve the sensitivity by one order of magnitude and start to take data in 2016.

In MEG II, the major background source will be the accidental overlap of a positron from normal muon decay and a random γ-ray. Therefore, the rejection of the accidental background events plays an important role. One of the major background sources is the Radiative Muon Decay (RMD). The Radiative Decay Counter (RDC) identifies the background γ-ray from RMD by detecting the associated low momentum positron. Simulation studies suggest that the RDC will improve the sensitivity by about 30 % and MEG II could reach the ultimate sensitivity of 4.0×10^{-14}. The details of the detector will be discussed in this thesis.

Contents

List of Figures

List of Tables

Chapter 1

Introduction

Particle physics is a field of study that explains what elementary constituents of matter are and what determines their behavior. Since J.J. Thomson discovered an electron as the first elementary particle in 1897, people have sought for a better model to describe our world.

The Standard Model, which has been developed since the beginning of the 20th century, is one of the most successful theories which explain physical phenomena. It contains three types of particles: spin-$\frac{1}{2}$ fermions (quarks and leptons), spin-1 gauge bosons and spin-0 Higgs boson. The particles in the standard model is summarized in Fig.1.1.

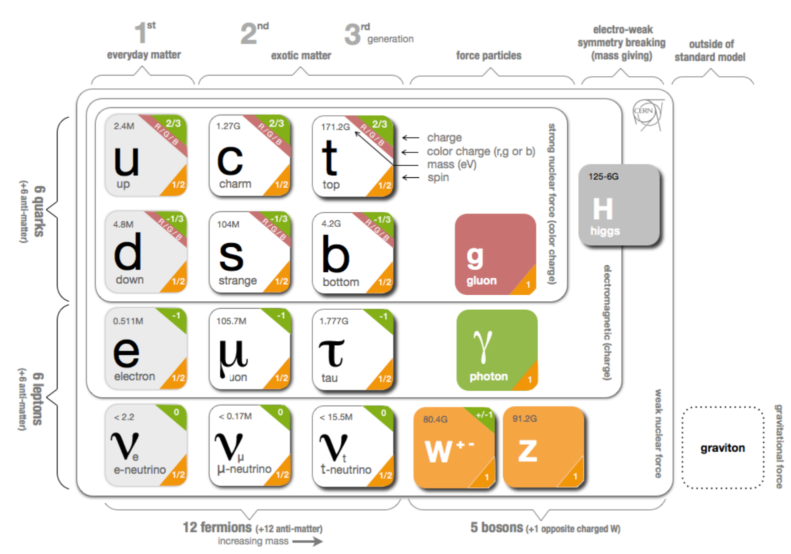

Fig. 1.1: List of particles in the Standard Model [2]

When particles interact with each other, we say that there is a force between them. Currently four forces (strong, weak, electromagnetic and gravity) are considered to be fundamental. The Standard Model describes strong, weak and electromagnetic forces as $\mathrm{SU(3)_C} \times \mathrm{SU(2)_L} \times \mathrm{U(1)_Y}$ symmetry and its spontaneous breaking. Gravity is not included in this model because it is negligibly small compared with the other forces. The discovery of the Higgs boson in 2012 strongly supported the model's validity since the particle was the last piece to be filled.

Although the Standard Model has been successful in explaining so many experimental results, there are still many unanswered questions and unnaturalnesses, such as dark matter and the hierarchy problem. It suggests that the Standard Model is not a final theory but just a low-energy effective theory. In this situation, new theories which replace the Standard Model at high energy scales have been proposed. They are called "physics Beyond the Standard Model " or "new physics". There are many promising candidates such as Grand Unified Theory (GUT) and SUperSYmmetry (SUSY). Charged Lepton Flavor Violation (cLFV) is a good probe to test new physics because the predicted branching ratios of cLFV decays depend on the model. Many of new physics models predict experimentally accessible branching ratios of the $\mu \to e\gamma$, the $\mu \to eee$, and the $\mu - e$ conversion while these processes are almost forbidden in the Standard Model. Confirming the presence of these processes implies the obvious existence of new physics and that is why they are called "golden channels".

Chapter 2

Theoretical Background

Muon was discovered in 1936 and found to be a replica of the electron with a heavier mass (105.7 MeV). It is classified as the second-generation charged lepton. Here we discuss the properties and the connection with new physics.

2.1 Muon Physics in the Standard Model

Interactions in the Standard Model are summarized in the form of a Lagrangian. Leptons do not have color charge so they don't have any strong interaction term. The quantum numbers of the second-generation Leptons are shown in this table:

- SECOND GENERATION -			
lepton	T_3	Y	Q
μ_L^-	-$\frac{1}{2}$	-1	-1
μ_R^-	0	-2	-1
ν_μ	$\frac{1}{2}$	-1	0

Here we consider tree-level terms (i.e. without loops) related to the muon in the Lagrangian.

$$\begin{aligned}\mathcal{L} = {} & \mathrm{e}\mu\gamma^\lambda\mu A_\lambda \\ & - \frac{g}{\sqrt{2}}(\overline{\nu}_{\mu L}\gamma^\lambda\mu_L W_\lambda^+ + \overline{\mu}_L\gamma^\lambda\nu_{\mu L}W_\lambda^-) \\ & - \sqrt{g^2+g'^2}\left\{\overline{\mu}_L\gamma^\lambda\left(-\frac{1}{2}+\sin^2\theta_W\right)\mu_L + \overline{\mu}_R\gamma^\lambda\sin^2\theta_W\mu_R\right\}Z_\lambda^0 \\ & - \frac{m_\mu}{v}\mu\mu\mathrm{H}\end{aligned} \tag{2.1}$$

The respective terms correspond to the interaction via photon, W boson, Z boson, and Higgs boson.

Table 2.1: Muon decay modes and their branching ratios [18]

Mode	Fraction	Confidence Level
$\mu^- \to e^-\overline{\nu}_e\nu_\mu$	$\simeq 100$ %	
$\mu^- \to e^-\overline{\nu}_e\nu_\mu\gamma$	(1.4 ± 0.4) %	
$\mu^- \to e^-\overline{\nu}_e\nu_\mu e^+e^-$	$(3.4 \pm 0.4) \times 10^{-5}$	
$\mu^- \to e^-\nu_e\overline{\nu}_\mu$	< 1.2 %	90 %
$\mu^- \to e^-\gamma$	$< 5.7 \times 10^{-13}$	90 %
$\mu^- \to e^-e^+e^-$	$< 1.0 \times 10^{-12}$	90 %
$\mu^- \to e^-2\gamma$	$< 7.2 \times 10^{-11}$	90 %

2.1.1 Decay Mode

As given in the second line of (2.1), the muon decay process in the Standard Model is described by V-A interaction (i.e. only left-handed muons interact via a charged-weak current interaction). The interaction is expressed as

$$\mathcal{L}_{Fermi} = \frac{G_F}{\sqrt{2}}\left[\overline{\nu}_e\gamma^\lambda(1-\gamma_5)\mu\right]\left[e\gamma_\lambda(1-\gamma_5)\nu_e\right] \tag{2.2}$$

and its differential decay rate is

$$\frac{d^2\Gamma}{dx\, d\cos\theta_e} = \frac{m_\mu^5 G_F^2}{192\pi^3}x^2\left[(3-2x) \pm P_\mu\cos\theta_e(2x-1)\right] \tag{2.3}$$

Here G_F is the Fermi coupling constant, x is defined as $x = E_e/W_{e\mu}$ (here $W_{e\mu}$ is the maximum electron energy: $W_{e\mu} = max(E_e) = (m_\mu^2 + m_e^2)/2m_\mu$), P_μ is the degree of muon polarization, and θ_e is the angle between muon spin and positron momentum. The dominant process: $\mu^- \to e^-\nu_e\overline{\nu}_\mu$ is called Michel decay. As mentioned later, the energy spectra of electrons from the Michel decay and of the gamma-ray from Radiative Muon Decay (RMD:$\mu^- \to e^-\overline{\nu}_e\nu_\mu\gamma$) are important to define the experimental requirements. The two spectra are shown in Fig.2.1, 2.2.

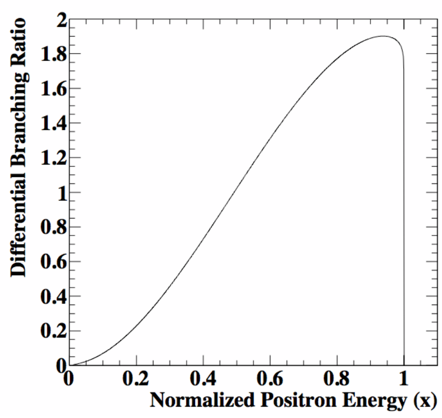

Fig. 2.1: Energy spectrum of the electrons from Michel decay

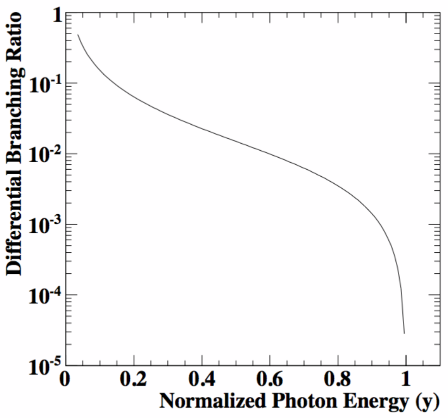

Fig. 2.2: Energy spectrum of gamma-rays from RMD

2.1.2 $\mu \to e\gamma$ in the Standard Model

The Standard Model forbids the charged Lepton Flavor Violation. However, the neutrino oscillation can induce the $\mu \to e\gamma$ decay. Here we introduce a lepton-mixing matrix, called Pontecorvo-Maki-Nakagawa-Sakata (PMNS) matrix.

$$U_{PMNS} = \begin{pmatrix} U_{e1} & U_{e2} & U_{e3} \\ U_{\mu 1} & U_{\mu 2} & U_{\mu 3} \\ U_{\tau 1} & U_{\tau 2} & U_{\tau 3} \end{pmatrix} \tag{2.4}$$

$$= \begin{pmatrix} 1 & 0 & 0 \\ 0 & c_{23} & s_{23} \\ 0 & -s_{23} & c_{23} \end{pmatrix} \begin{pmatrix} c_{13} & 0 & s_{13}e^{-i\delta} \\ 0 & 1 & s_{23} \\ -s_{13}e^{i\delta} & 0 & c_{13} \end{pmatrix} \begin{pmatrix} c_{12} & s_{12} & 0 \\ -s_{12} & c_{12} & 0 \\ 0 & 0 & 1 \end{pmatrix} \tag{2.5}$$

where $c_{ij} = \cos\theta_{ij}$, $s_{ij} = \sin\theta_{ij}$ and θ_{ij} is a mixing angle. With the neutrino mixing, the $\mu^+ \to e^+\gamma$ decay can be induced as shown Fig.2.3 but the calculated branching ratio is negligibly small:

$$\mathcal{B}(\mu \to e\gamma) = \frac{3\alpha}{32\pi} \left| \sum_{i=2,3} U^*_{\mu i} U_{ei} \frac{\Delta m^2_{i1}}{M^2_W} \right|^2 \simeq 10^{-54} \tag{2.6}$$

Here, U_{ij} is the PMNS matrix and Δm^2_{ij} are the mass squared differences between the neutrinos. The sensitivity of the experiment today is $O(10^{-13})$ and the decay has not been observed.

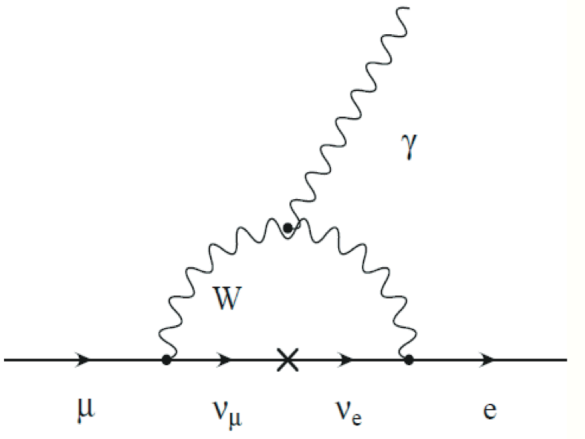

Fig. 2.3: $\mu \to e\gamma$ decay in the Standard Model

2.2 Muon Physics Beyond the Standard Model

The Standard Model so excellently explains almost all the experimental observations. However, there are still many unsatisfied points for it to be the final theory. We will briefly discuss the main problems in the Standard Model and hypotheses which try to solve them in this section.

2.2.1 Grand Unified Theory

While the Standard Model successfully unified electromagnetic and weak interaction based on the $\mathrm{SU(2)_L \times U(1)_Y}$ group, the magnitudes of coupling constants are different and independent. This is obviously unsatisfactory and the next step is to extend the gauge group and try to unify all coupling constants. The Grand Unified Theory (GUT) is a model which tries to unify electroweak interaction and strong interaction, assuming the $\mathrm{SU(3)_C \times SU(2)_L \times U(1)_Y}$ group is a part of a larger group G (i.e. $\mathrm{G \supset SU(3)_C \times SU(2)_L \times U(1)_Y}$). The simplest group is SU(5) so it can be considered the minimal extension of the Standard Model. It puts the 15 fermions of the first generation into 5-plet and 10-plet:

$$\psi_5 = \begin{pmatrix} d_g^c \\ d_r^c \\ d_b^c \\ e^- \\ \nu \end{pmatrix}_L , \quad \psi_{10} = \begin{pmatrix} 0 & u_b^c & -u_r^c & u_g & d_g \\ & 0 & u_g^c & u_r & d_r \\ & & 0 & u_b & d_b \\ & & & 0 & e^+ \\ & & & & 0 \end{pmatrix}_L \tag{2.7}$$

The superscription C indicates the charge conjugation. This expression enables us to explain the charge quantization and to predict the value of the electroweak mixing angle (i.e. $\sin^2\theta_W$). However, predictions of the minimal SU(5) is inconsistent with the experimental result such as the proton decay search at KAMIOKANDE. The unified coupling constant cannot be got with minimal SU(5). Although the minimal SU(5) model is already excluded, by introducing new physics the experimental phenomena can be explained and the unification of coupling constants can also be obtained.

2.2.2 Hierarchy Problem and Supersymmetry

If we assume the Standard Model is a low energy effective theory, a certain energy scale Λ up to which the Standard Model is valid exists. The scale is called cut-off and considered to be much larger than the electroweak scale, such as 10^{15} GeV (GUT scale) or 10^{19} GeV (Planck scale).

Although the gauge symmetry implies zero-mass gauge bosons and the chiral symmetry accounts for the small mass of fermions, there is no symmetry to protect the mass of the Higgs boson. As a result, the Higgs mass gets a large quantum correction and can easily reach the cut-off scale. Actually the observed Higgs mass-squared $m_h^2 = 2\mu^2$ has the quadratic divergence Λ^2:

$$2\mu^2 = 2\mu_0^2 - c\Lambda^2$$

$2\mu_0^2$ is the bare mass-squared, and c is a constant. In order to get a 10^2 GeV Higgs mass on the left hand, the two terms on the right hand should cancel out. Assuming $\Lambda \sim 10^{15}$ GeV and $c \sim \alpha \sim 10^{-2}$, it requires a fine tuning of the bare parameter at the precision of $(\frac{2\mu^2}{c\Lambda^2}) \sim 10^{-26}$. This is quite unnatural and it is difficult to recognize the Standard Model as the final theory.

The application of supersymmetry (SUSY) to the Standard Model is an attractive solution. The SUSY is a symmetry which connects particles whose spin is different by $\frac{1}{2}$. The SUSY transformation is given by

$$Q|Fermion\rangle = |Boson\rangle \tag{2.8}$$

$$Q^\dagger|Boson\rangle = |Fermion\rangle \tag{2.9}$$

where Q is a SUSY generator or supercharge. Since supersymmetry is independent of the other internal symmetries, the connected pair of particles carry the same quantum numbers except for the spin. In addition, the difference of spin statistics gives the opposite sign to the Feynman diagram with a loop. As the result, the quadratic divergence which derives from Fig. 2.4a and Fig. 2.4b will cancel out.

Although SUSY is an attractive idea, it should be broken. That is because we have never observed bosons which are the partners of quarks or leptons with the same mass. Due to the SUSY breaking, the Higgs mass has a logarithmic divergence $M_{SUSY}^2 \log \Lambda$. M_{SUSY} is the energy scale where the SUSY breaking takes place. If we assume M_{SUSY} is sufficiently small ($\alpha M_{SUSY}^2 \leq M_W^2 \rightarrow M_{SUSY} \leq$ 1TeV), we are still free from the divergence.

Table 2.2: Particles in the MSSM

Particle	Spin	Superpartner	Spin
quark	1/2	squark	0
lepton	1/2	slepton	0
gluon	1	gluino	1/2
W boson	1	wino	1/2
Z boson	1	bino	1/2
Higgs boson	0	Higgsino	1/2

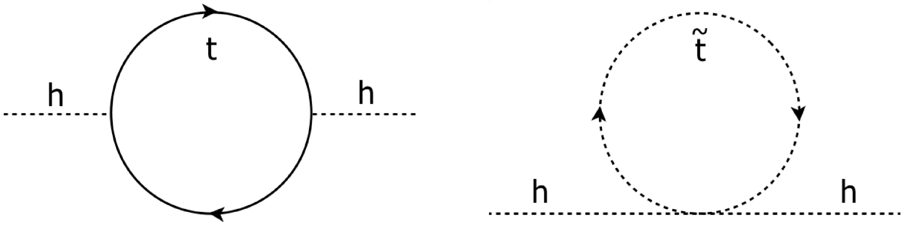

(a) radiative correction to the Higgs mass from top quark loop

(b) correction from a loop of the superpartner of top quark (stop)

Fig. 2.4: one-loop contributions to Higgs mass

In the Minimal Supersymmetric extension of the Standard Model (MSSM), we require two Higgs potentials H_1, H_2 and they are expressed as

$$H_1 = \frac{\mathrm{v}_1}{\sqrt{2}} \begin{pmatrix} 1 \\ 0 \end{pmatrix} \tag{2.10}$$

$$H_2 = \frac{\mathrm{v}_2}{\sqrt{2}} \begin{pmatrix} 0 \\ 1 \end{pmatrix} \tag{2.11}$$

in a vacuum with $SU(2) \times U(1)$ breaking. $\tan\beta$ is defined as the ratio of the two Higgs vacuum expectation values: $\tan\beta = \mathrm{v}_2/\mathrm{v}_1$.

2.2.3 See-Saw Mechanism

Although the neutrino mass is strictly zero in the Standard Model, the observation of neutrino oscillation strongly suggests the non-zero neutrino mass. There are three possible types of neutrino mass: Pure Dirac, Pseudo-Dirac and Seesaw. The first case has only Dirac masses, and the second case also includes small Majorana masses. The third Seesaw is the extreme scenario where Majorana masses are much higher than Dirac ones. The most general mass term is expressed as

$$\begin{aligned}\mathcal{L}_m &= -\frac{1}{2}m_R\overline{(\nu_R)^c}\nu_R - \frac{1}{2}m_L\overline{(\nu_L)^c}\nu_L - m_D\overline{\nu_R}\nu_L + h.c. \\ &= -\frac{1}{2}\begin{pmatrix}\overline{(\nu_L)^c} & \overline{\nu_R}\end{pmatrix}\begin{pmatrix}m_L & m_D \\ m_D & m_R\end{pmatrix}\begin{pmatrix}\nu_L \\ (\nu_R)^c\end{pmatrix} + h.c. \qquad (2.12)\end{aligned}$$

ν_R and ν_L are right- and left-handed neutrinos. If we assume that $m_L = 0$ and $m_D \gg m_R$, the mass matrix becomes

$$M_\nu = \begin{pmatrix}0 & m_D \\ m_D & m_R\end{pmatrix} \qquad (2.13)$$

and its eigenvalues m_s,m_a are

$$m_s \simeq m_R \qquad (2.14)$$

$$m_a \simeq \frac{m_D^2}{m_R} \qquad (2.15)$$

From the two eigenvalues, we obtain

$$m_s \cdot m_a \simeq m_D^2 \qquad (2.16)$$

This relation means that if the mass m_R is much bigger than m_D (weak scale), m_a gets much smaller than m_D, which could explain why the neutrino mass is very small.

2.2.4 $\mu \to e\gamma$ as a Probe of New Physics

As mentioned above, the Standard Model forbids cLFV process and the $\mu \to e\gamma$ decay cannot be experimentally observed. On the other hand, new physics like the supersymmetric grand unified theory (SUSY-GUT) or supersymmetric seesaw model (SUSY-seesaw) introduce large cLFV and the rate of the $\mu \to e\gamma$ reaches an observable level through loop diagrams such as the one in Fig.2.5. TeV-scale particles carry flavor violating couplings and the branching ration of $\mu \to e\gamma$ is rather enhanced.

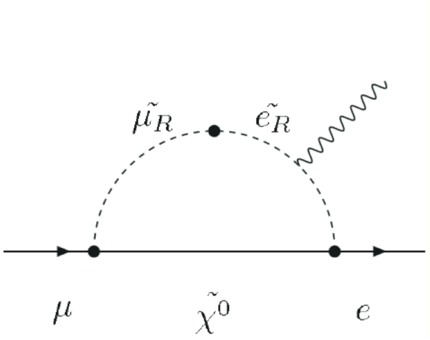

Fig. 2.5: one of the diagrams contributing to $\mu \to e\gamma$ decay process in BSM

$\mathcal{B}(\mu^+ \to e^+\gamma)$ as a function of the right-handed selectron mass $m_{\tilde{e}_R}$ in SU(5) SUSY- GUT and SU(10) SUSY - GUT model are shown in Fig.2.6, 2.7. The gaugino mass M_2 is set as SUSY input parameters.

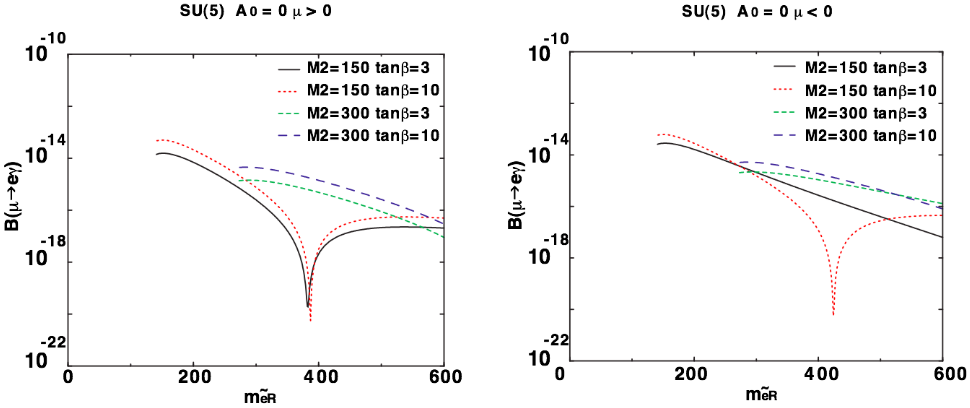

Fig. 2.6: Predicted $\mathcal{B}(\mu^+ \to e^+\gamma)$ in SU(5) SUSY GUT model [4]

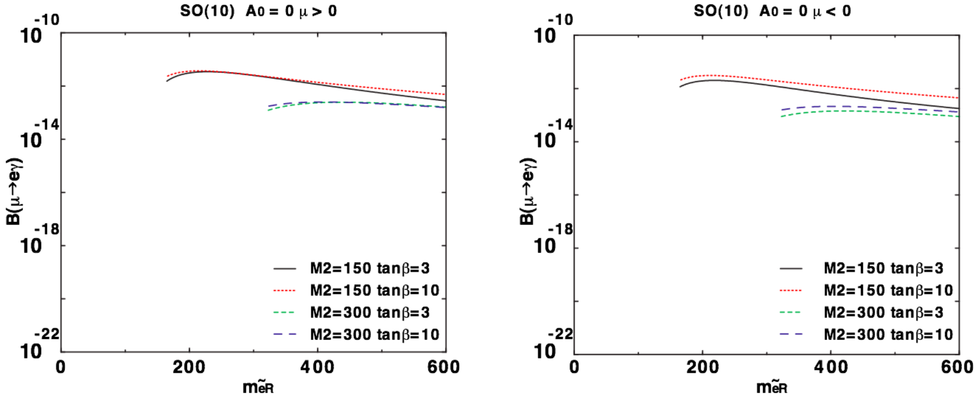

Fig. 2.7: Predicted $\mathcal{B}(\mu^+ \to e^+\gamma)$ in SU(10) SUSY GUT model [4]

In Fig. 2.8, the correlation of branching ratios for two cLFV processes in SUSY-seesaw are shown. Considering that the neutrino mixing angle is $\theta_{13} \sim 9°$, the relevant region is confined to the magenta areas only.

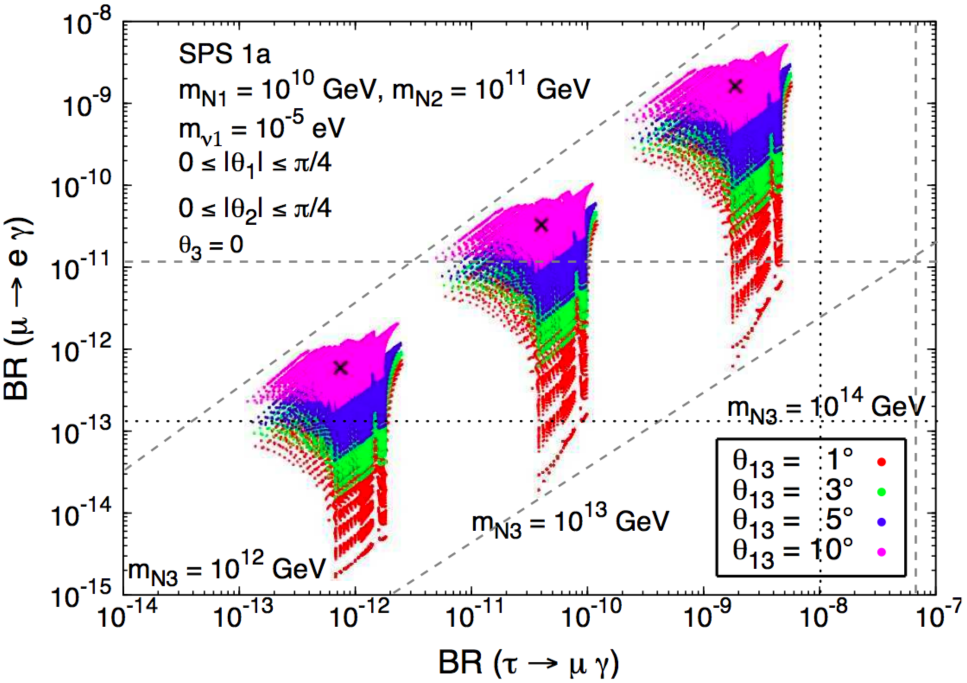

Fig. 2.8: Correlation between $B(\mu \to e\gamma)$ and $B(\tau \to \mu\gamma)$ with SUSY seesaw [5]

The $\mu \to e\gamma$ decay rate of $O(10^{-14})$ is the level the MEG II experiment can reach. As explained, the $\mu \to e\gamma$ process has no background from the Standard Model. That is, the observation of $\mu \to e\gamma$ means the obvious existence of new physics.

Chapter 3

MEG II Experiment

The first search for the "golden" channel $\mu^+ \to e^+\gamma$ began in 1947 with cosmic muons. From the 1970s, the high-intensity μ^+ beams became available. In 1999 the MEGA experiment used muons from the surface muon beam at the Los Alamos Meson Physics Facility and set the upper limit of $\mathcal{B} < 1.2 \times 10^{-11}$ (90% C.L.)[19]. The Mu to E Gamma (MEG) experiment at the Paul Scherrer Institute (PSI) started data taking in 2008 and set the limit $\mathcal{B} < 5.7 \times 10^{-13}$ (90% C.L.) by analyzing the first half of data [1]. The MEG experiment will be upgraded and will aim at a sensitivity of 4×10^{-14}. In this chapter, the MEG experiment will be reviewed and the detail of the upgrade experiment (called MEG II) will be discussed in this chapter.

3.1 MEG Experiment

An experiment to search for cLFV process $\mu^+ \to e^+\gamma$ with a high sensitivity was proposed by four Japanese and one Russian institutions, and the research committee in the PSI approved it and the MEG experiment started in 1999 [8]. Now the MEG collaboration consists of about sixty physicists from Japan, Switzerland, Italy, Russia and the USA. In the PSI, the world's most intense DC muon beam is available. This powerful muon beam enables us to search for rare decays such as $\mu^+ \to e^+\gamma$.

3.1.1 Signal and Backgrounds

Properties of $\mu \to e\gamma$

The muon beam is stopped on a target. The signal event from stopped muons is beautifully simple :

- a two-body decay into a positron and gamma-ray

- the two particles have an equal energy of 52.8 MeV (half of the muon mass)
- the two particles are emitted time-coincidently
- the two particles are emitted with an angle of 180° between them

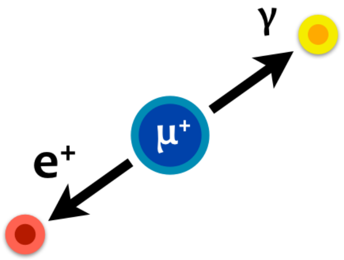

Fig. 3.1: $\mu^+ \rightarrow e^+\gamma$ decay from stopped muon

Therefore, the basic idea of the MEG experiment is to precisely measure the positron energy E_e, the gamma-ray energy E_γ, the relative timing $t_{e\gamma}$ between them, and the opening angle $\Theta_{e\gamma}$. The expected number of signal events (N_{sig}) is expressed as

$$N_{sig} = R_\mu \times T \times \mathcal{B} \times \Omega \times \epsilon_\gamma \times \epsilon_e \times \epsilon_s \tag{3.1}$$

where R_μ is the muon stopping rate, Ω is the solid angle covered by the gamma-ray and positron detectors, T is the measurement time, the ϵ_γ and ϵ_e are efficiencies of these detectors, and ϵ_s is the efficiency of the selection criteria.

Background Events

There are two major backgrounds in the $\mu^+ \rightarrow e^+\gamma$ search. One is a physics background from a Radiative Muon Decay (RMD: $\mu^+ \rightarrow e^+\nu_e\overline{\nu}_\mu\gamma$), where the positron and gamma-ray are emitted back-to-back and two neutrinos carry off small energy (Fig.3.2). The other is an accidental overlap of a positron from normal muon decay and a random gamma-ray. The uncorrelated gamma-ray mainly comes from an RMD or a positron annihilation in flight (AIF). The accidental background is dominant and it is determined by the detector resolutions of the MEG experiment. The expected number of accidental background events (N_{acc}) is expressed as

$$N_{acc} \propto R_\mu^2 \times (\Delta E)_\gamma^2 \times \Delta P_e \times (\Delta\Theta)_{e\gamma}^2 \times \Delta t_{e\gamma} \times T \tag{3.2}$$

where ΔE, ΔP_e, $\Delta\Theta$ and $\Delta t_{e\gamma}$ are the experimental resolutions for the photon energy, the muon momentum, the opening angle, and the relative timing.

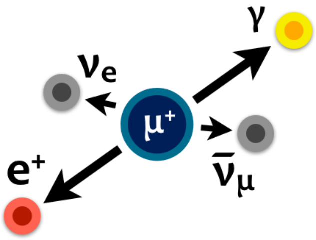

Fig. 3.2: physics background

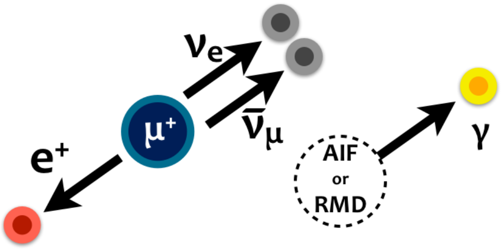

Fig. 3.3: accidental background

$\mu \to e\gamma$ Search Requirements

While we need high-rate muon beam to get enough statistics, the high-rate stopped muon decay ($> 10^7$/sec) increases the number of the accidental background events more than the one of signal events as we can see in (3.1) and (3.2). From a point of view of the accidental background suppression, a DC muon beam is better than a pulsed beam.

As can be seen in Fig.2.1, the energy spectrum of positrons from Michel decay have a its maximum around the signal region. It means that the positron spectrometer has to measure high positron hit rates ($\sim 10^7 - 10^8$/sec). While the improvement of the positron energy resolution is not efficient for reducing accidental background events, a photon detector with a high energy resolution can strongly suppress the accidental background events since the energy spectrum of background gamma-ray from RMD falls rapidly for the signal region as shown in Fig.2.2. Summarizing them, we need

- a high intensity DC muon beam
- a positron spectrometer which can measure high-rate positrons precisely
- a gamma-ray detector which has a high energy resolution

In addition to the good resolutions of detectors, an active tag of background events can be another possibility to further improve the search sensitivity. Based on this concept, the MEG II experiment employs a new detector, radiative decay counter (RDC), which will be later described in detail.

MEG Experimental Apparatus Overview

The MEG experiment, whose schematic view is shown in Fig.3.4, is designed to meet the requirements above. A high intensity muon beam in the π-E5 beam line at PSI is brought to the stopping target in the MEG detector at $3 \times 10^7 \mu^+$stops/sec. Emitted Gamma-rays are measured by a liquid xenon scintillation detector. Positrons are observed by a spectrometer composed of low material drift chambers and scintillation counters which is placed in a gradient magnetic field.

The coordinate system (x, y, z) is defined as follows. The origin is the center of the spectrometer magnet where the stopping target is located. The z-axis is the direction along the μ^+ beam axis and the y-axis points vertically upward.

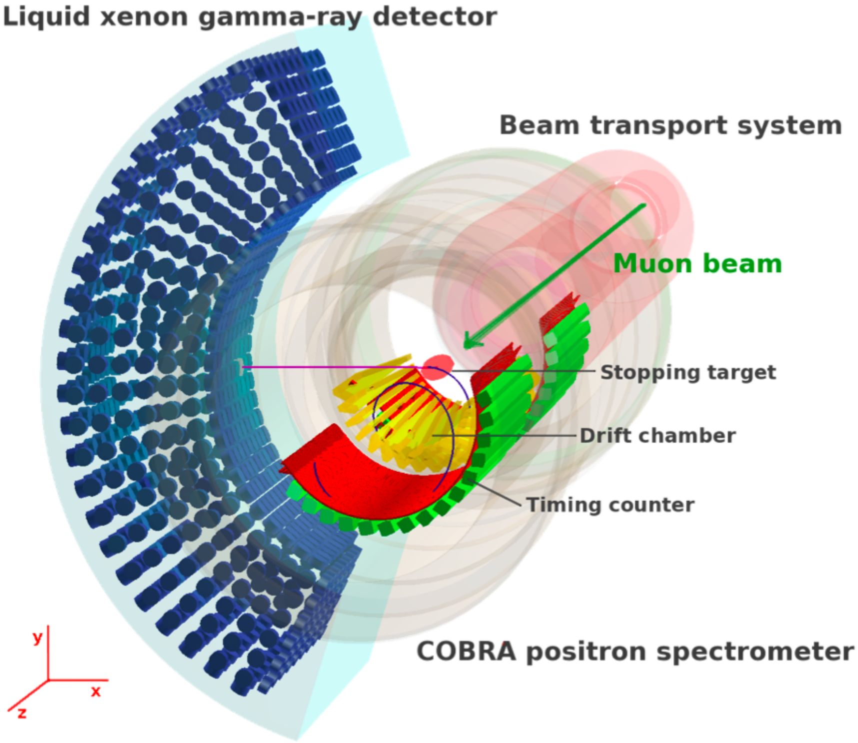

Fig. 3.4: A schematic view of the MEG experimental apparatus

3.1.2 Beam and Target

Surface μ^+ beam

The PSI runs a 590 MeV proton cyclotron with a maximum current of 2.3 mA (1.36 MW), as shown in Fig.3.5.

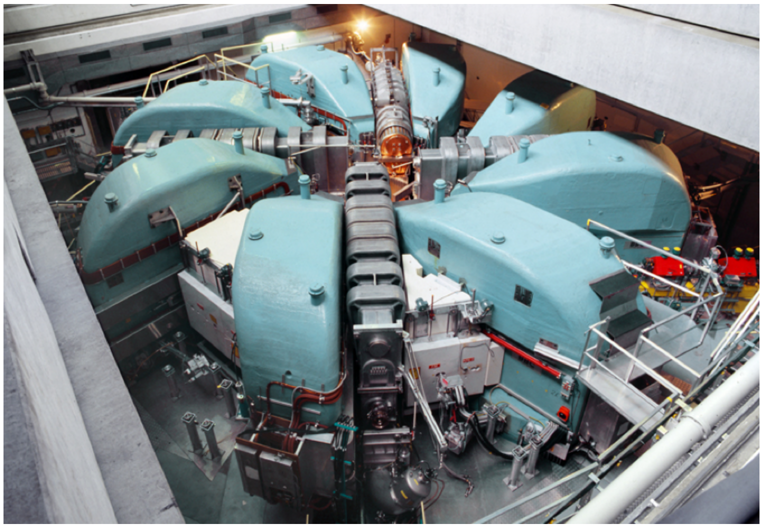

Fig. 3.5: The 590 MeV proton ring cyclotron which has four accelerator cavities (gray) and eight sector magnets (green)

The π-E5 channel extracts pions and muons produced in the target E in the primary proton beam (Fig.3.8). The extracted muons for the MEG experiment are so called "surface muons" and they are produced on the surface of the production target. Surface muons have a mean momentum of 28 MeV/c with a spread of 5-7% (FWHM).

The beam from π-E5 is brought to the MEG detector by a beam transport system shown in Fig.3.6. There are two main roles of the system: reducing the amount of beam contamination and adjusting the muon momentum. The system consists of Triplet I (first quadrupole triplet), a Wien filter, Triplet Ⅱ (second quadrupole triplet) and a beam transport solenoid (BTS). The Triplet I couples to the π-E5 channel. The Wien filter separates muons from contamination positrons by 7.5σ (12 cm) with crossing magnetic field (133 G) and electric field (195 kV). Triplet Ⅱ refocuses the beam at the collimator system. The magnetic field of the BTS is designed to minimize the beam spot size on the stopping target by adjusting the oscillation of the beam profile. In the BTS a muon momentum degrader made of a 300 μm Mylar film is placed in order for muons to stop on the target efficiently.

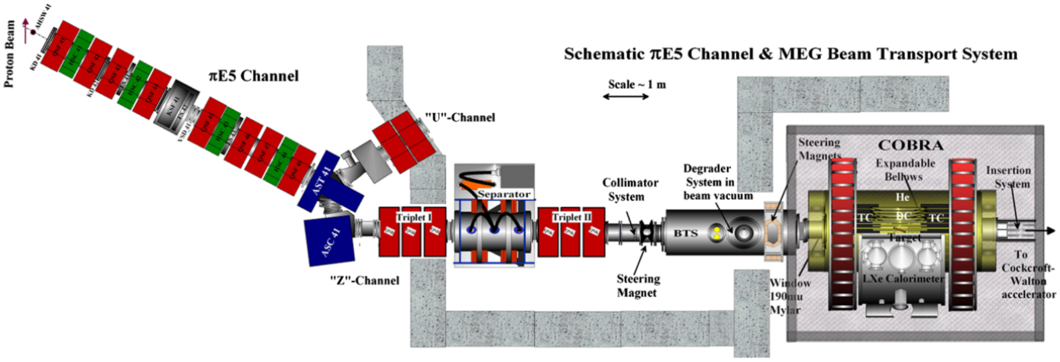

Fig. 3.6: Schematic view of the πE5 channel and the MEG beam transport system

μ^+ stopping target

The muon stopping target is made of a polyethylene-polyester film with 205 μm thickness (Fig.3.7). It has six holes of 10 mm diameter to monitor the target position. It has an angle of 20.5° with respect to the beam axis in order to obtain a good stopping power while keeping the multiple scattering of the positron and the production of background gamma-rays due to positron annihilation in flight to a minimum.

Fig. 3.7: μ^+ stopping target

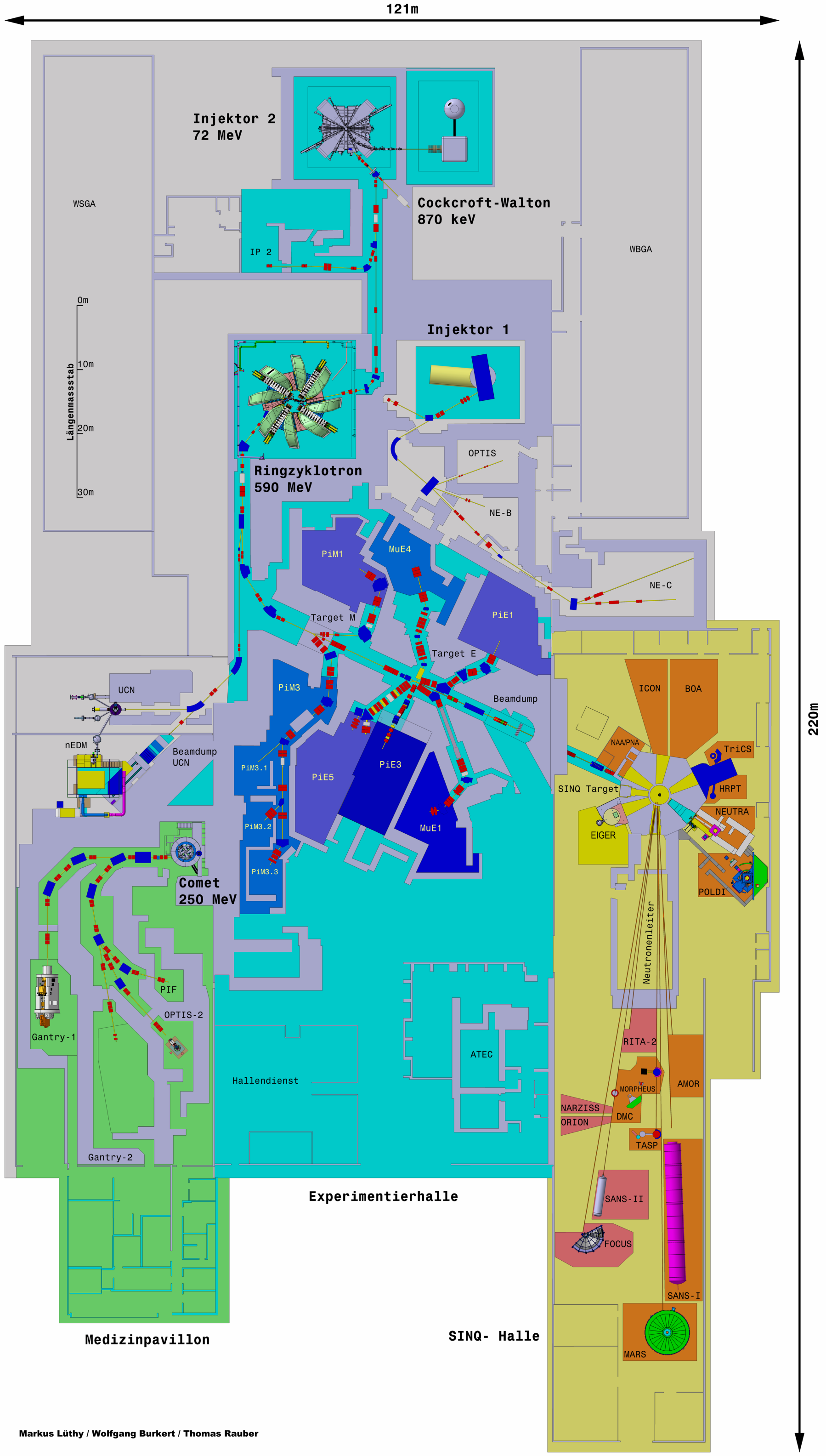

Markus Lüthy / Wolfgang Burkert / Thomas Rauber

Fig. 3.8: The cyclotron facility and the beam lines at the PSI. The MEG experiment is carried out in πE5 which is located at the center.

3.1.3 Positron Spectrometer

To fulfill the requirement of the MEG experiment, the positron spectrometer must satisfy these conditions:

- stable operation under high positron hit rate
- good resolution of positron momentum, direction and timing

In order to suppress multiple coulomb scattering of positron and suppress gamma-ray production from position annihilation in flight, we also require

- a low mass tracker

The spectrometer consists of three parts: a superconducting solenoidal magnet, drift chambers, and timing counters.

Constant projected Bending Radius (COBRA) magnet

The COBRA magnet is thin enough to allow the signal gamma-ray traverse it and reach the LXe gamma-ray detector placed outside the magnet. To meet the first requirement, a thin wall superconducting magnet was developed (Fig.3.9, Fig.3.10). The step structure solenoid is composed of five coils with three different radii and generates a gradient magnetic field as can be seen in Fig.3.11.

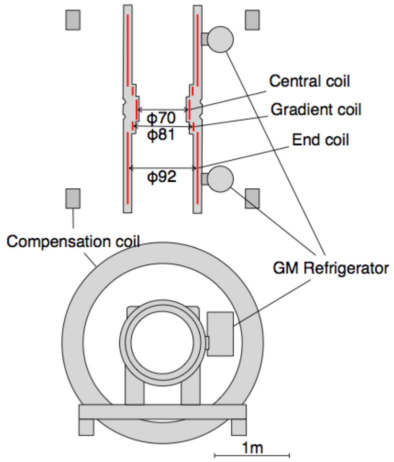

Fig. 3.9: Layout of the COBRA

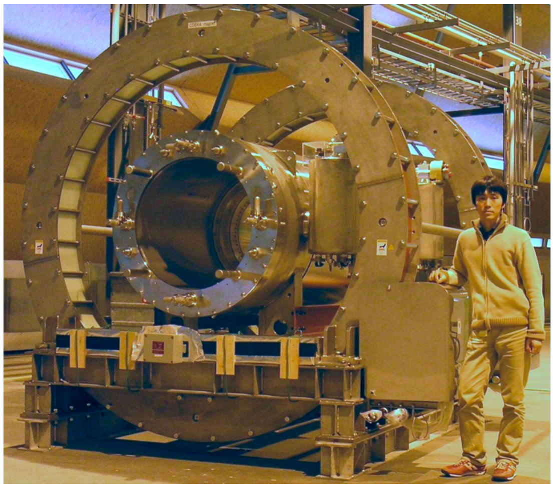

Fig. 3.10: Picture of the COBRA

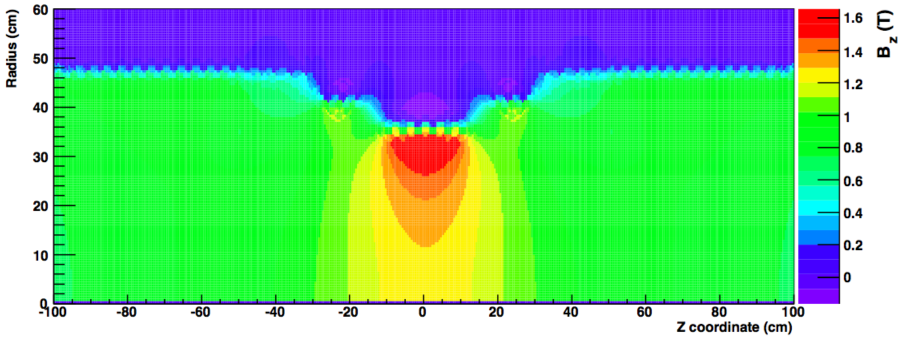

Fig. 3.11: COBRA z-direction magnetic field

The gradient magnetic field enables positrons with the same momentum to have trajectories with a constant projected bending radius regardless of their emission angles, as seen in Fig3.12(d). Thanks to this property, the positrons can be swept out more quickly from the sensitive detector volume, as can be seen in Fig.3.12(a) and Fig3.12(c). Accordingly, the drift chambers can be positioned in a narrow radial region corresponding to high momentum positrons only, and it leads to a reduced positron hit rate without losing signal efficiency.

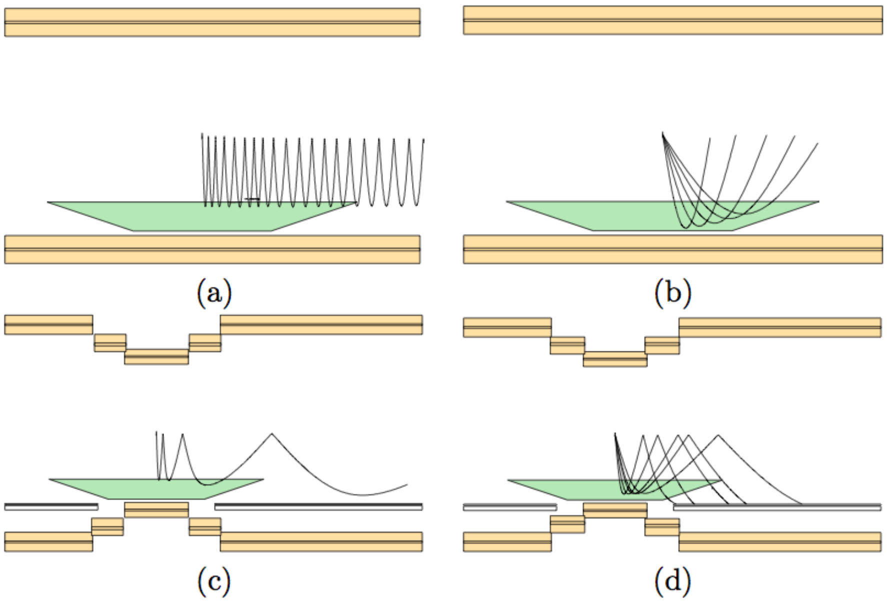

Fig. 3.12: Concept of COnstant projected Bending RAdius spectrometer. (a) and (b) show trajectories of positrons with a uniform magnetic field. (c) and (d) are the ones with COBRA.

Drift Chambers

A widespread device used to measure a charged particle track is the drift chamber. In the MEG, positron trajectories are measured with sixteen drift chambers as can be seen in Fig.3.13 and Fig.3.14. Because the tracking ability is limited by multiple coulomb scattering, the gas filled inside the chambers are a light gas mixture of helium and ethane (1:1). The low-mass chamber ($\sim 1.7 \times 10^{-3} X_0$) is also helpful for suppressing background gamma production from positron annihilation.

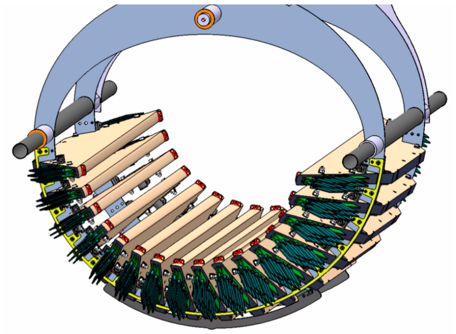

Fig. 3.13: Schematic view of drift chambers

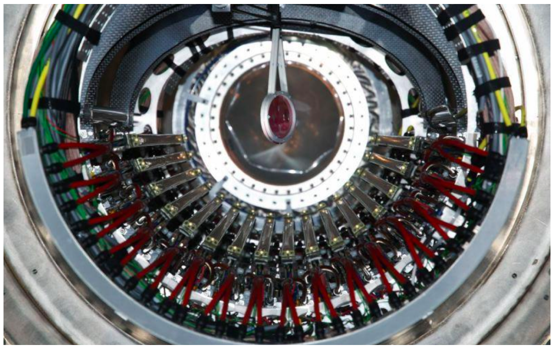

Fig. 3.14: Picture of drift chambers

Each chamber has a two-layer structure and the drift cells are staggered (Fig.3.15). The chamber walls are made of 12.5 μm polyimide films with aluminum deposition and they work as cathodes. The cathode of the cell consists of four strips with a zig-zag pattern (Fig.3.16). Since the anode wires are all mounted along the z-direction, the positron's hit z-position is reconstructed using the charge information. While the z-position is roughly estimated by the charge observed at both ends of the anode wire, a more precise z-position reconstruction is provided by the ratio of the induced charges of the four strips.

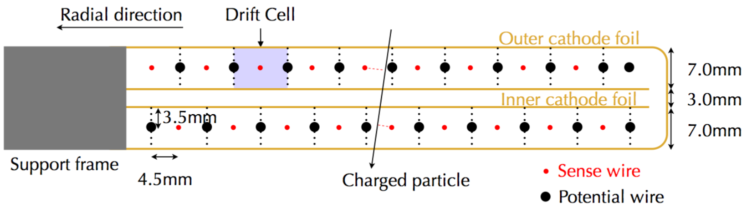

Fig. 3.15: Sectional view of a drift chamber

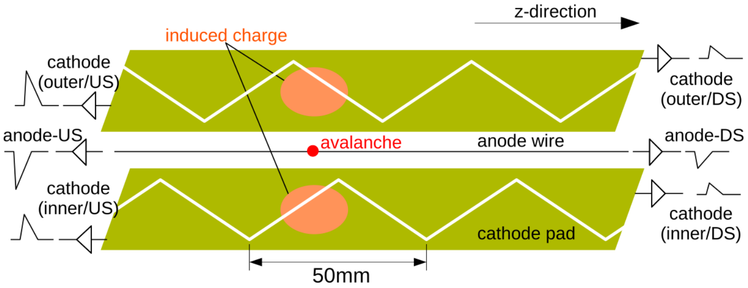

Fig. 3.16: Concept of positron z-reconstruction

Timing Counters

While the drift chamber shows a good performance as a tracking device, it does not have enough time resolution for the MEG experiment, that is why there is an additional detector for timing measurements, the so-called timing counter system. It consists of 15 plastic scintillation bars and 128 plastic scintillation fibers as shown in Fig.3.17 and Fig.3.18. The former are used for precise time measurement of ~50 psec, and the latter are used for z-position measurement of the positron hit. Two sets of the timing counter systems are installed at the upstream and downstream sides of the drift chambers.

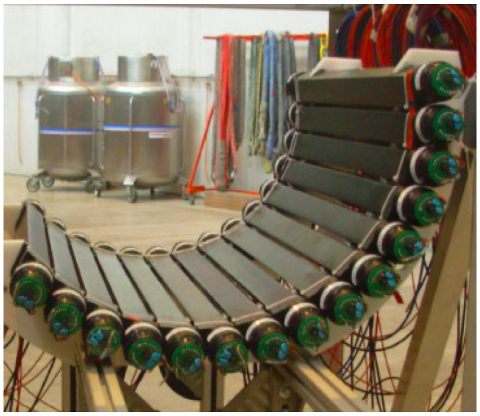

Fig. 3.17: Plastic scintillation bars for time measurement.

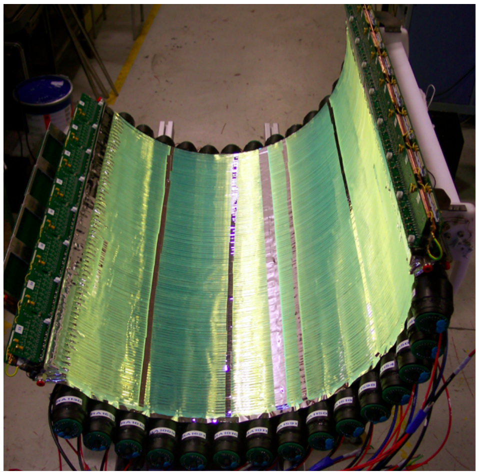

Fig. 3.18: Plastic scintillation fibers for z-position measurement

3.1.4 Gamma-ray Detector

As with the positron spectrometer, a gamma-ray detector plays an important role for $\mu^+ \rightarrow e^+\gamma$ detection. One of main features of the MEG experiment is that over 800 litter liquid xenon is used as the scintillation detector. The scintillation light is read out by photomultiplier tubes.

Liquid Xenon

The basic properties of liquid xenon is summarized in the following table.

Table 3.1: Properties of liquid xenon

Atomic Number	54
Atomic Weight	131
Density at 161.35 K	2.978 g/cm^3
Radiation length	2.77 cm
Critical Energy	10.5 MeV
Mollier radius	4.1 cm
Boiling point	165 K
Melting point	16 1K
wavelength	
178±14 nm W$_{ph}$ for electrons	21.6 eV [10]
Decay time (recombination)	45 nsec [11]
Decay time (fast components)	4.2 nsec [11]
Decay time (slow components)	22 nsec [11]
Absorption length	>100 cm
scatter length	29 cm to 50 cm

As a scintillation medium, liquid xenon has good characteristics:

- high light yield
- fast decay time
- short radiation length
- uniformity

Thanks to these advantages, a compact gamma-ray detector which has good energy and time resolutions can be realized.

When a particle passes through liquid xenon, Xe^* (excited state) or Xe^+ (ion) is produced. In either case, the scintillation process is considered to be de-excitation of dimers (Xe_2^*). In the ion case, the process is

$$Xe^* + Xe \rightarrow Xe_2^+ \tag{3.3}$$

$$Xe_2^* \rightarrow 2Xe + h\nu \tag{3.4}$$

On the other hand, the ion emits photon through following process:

$$Xe^+ + Xe^* \rightarrow Xe_2^+ \tag{3.5}$$

$$Xe_2^+ + e^- \rightarrow Xe^{**} + Xe \tag{3.6}$$

$$Xe^{**} \rightarrow Xe^* + \text{heat} \tag{3.7}$$

$$Xe^* + Xe + Xe \rightarrow Xe_2^* + Xe \tag{3.8}$$

$$Xe_2^* \rightarrow 2Xe + h\nu \tag{3.9}$$

The feature of the photons from the emission processes is useful to achieve a good energy resolution because photons from Xe_2^* cannot be absorbed by Xe.

Photomultiplier tube

Since the scintillation light of liquid xenon has a peak at 175 nm [12], the photomultiplier tubes must be sensitive to the vacuum ultraviolet. The MEG collaboration and Hamamatsu Photonics developed a 2-inch VUV-sensitive photomultiplier, R9869 (Fig.3.19), which has a quartz window instead of normal glass one. Thanks to the new type of window, 80 % of the scintillation light can pass.

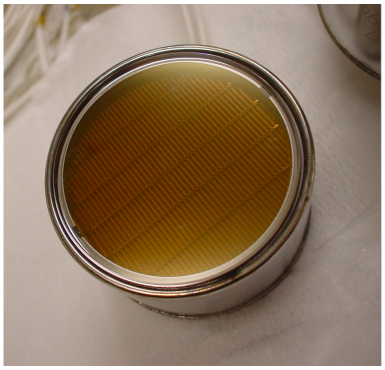

Fig. 3.19: R9869

Detector design

Over 800 litter liquid xenon fill a C-shaped cryostat shown in Fig.3.20. 846 photomultiplier tubes surround the active volume and they collect the scintillation light. It covers approximately 10 % of the solid angle seen by the muon stopping target.

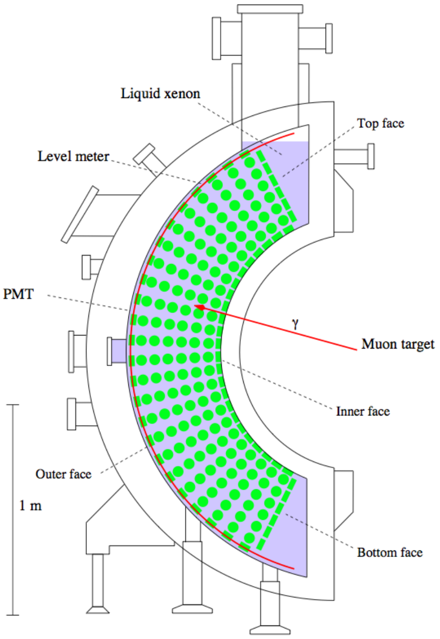

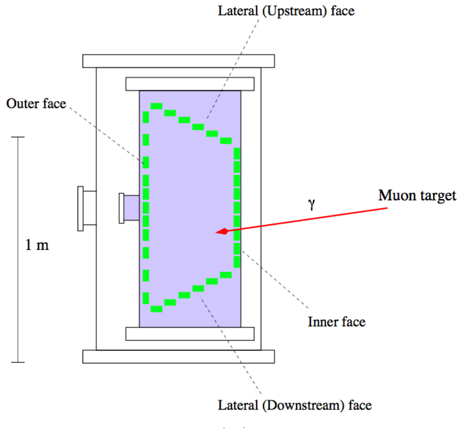

Fig. 3.20: Side view of the liquid xenon detector

Fig. 3.21: Top view of the liquid xenon detector

3.1.5 Data Acquisition System

The MEG experiment records the waveforms from all the detectors to obtain the precise information such as the charge, the time, the baseline, and the pileup with a fast digitizer called Domino Ring Sampler (DRS) [13]. The DRS has been developed at the PSI and the latest version is called "DRS4". Each DRS4 chip (Fig.3.22) has eight data readout channels.

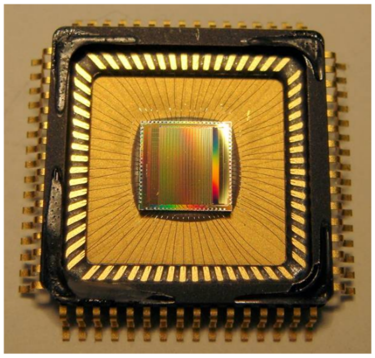

Fig. 3.22: DRS chip

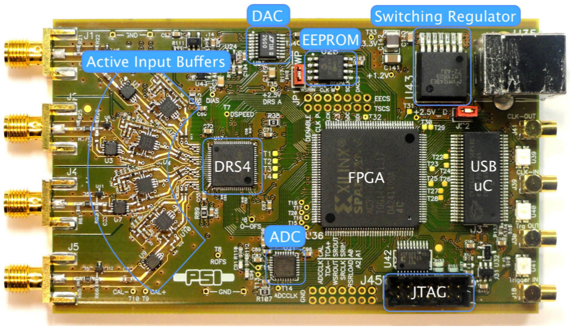

Fig. 3.23: DRS4 evaluation board [14]

Fig.3.24 shows the principle of the DRS. Each channel of the DRS has 1024 capacitive sampling cells. The sampling speed is determined by the series-connected inverters and the highest speed is 5 GHz. Due to the rotating signal, the sampling frequency continuously runs on the inverter chain and it is called "domino wave". When an external trigger signal comes, the domino wave stops and the waveform stored is read out with a shift resister at lower frequency and digitized by an external 12 bit FADC .

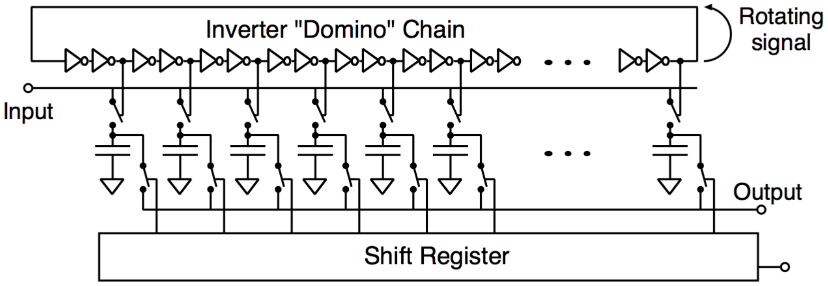

Fig. 3.24: Conceptual view of the DRS principle

The data was acquired with a sampling speed of 1.6GHz for the liquid xenon detector and timing counter and 0.8GHz for the drift chambers.

3.2 Upgrade Experiment: MEG II

We achieved a sensitivity of 7.7×10^{-13} with the first half of the data in the MEG experiment. To achieve a higher sensitivity, more statistic is necessary. However, we do not expect a significant improvement by just increasing the statistics because of increasing background events in the signal region. Accordingly, we will require

- higher intensity of muon beam
- detectors able to operate with the increased hit rate
- detectors with higher energy, time, angular resolutions

for the upgrade experiment, MEG II.

3.2.1 Key Points in the Upgrade

The improvement in the upgrade is summarized as follows (numbers refer to the numbers shown in Fig.3.25)

- the increased number of stopping muons on the target (1)

- the thinner stopping target (2)
- a new positron tracker with smaller radiation length, larger acceptance and higher resolutions (3,4)
- the gamma-ray detector with with higher resolutions and a better detection efficiency (6,7)
- active tagging of background events (8)
- integration of splitter, trigger and DAQ

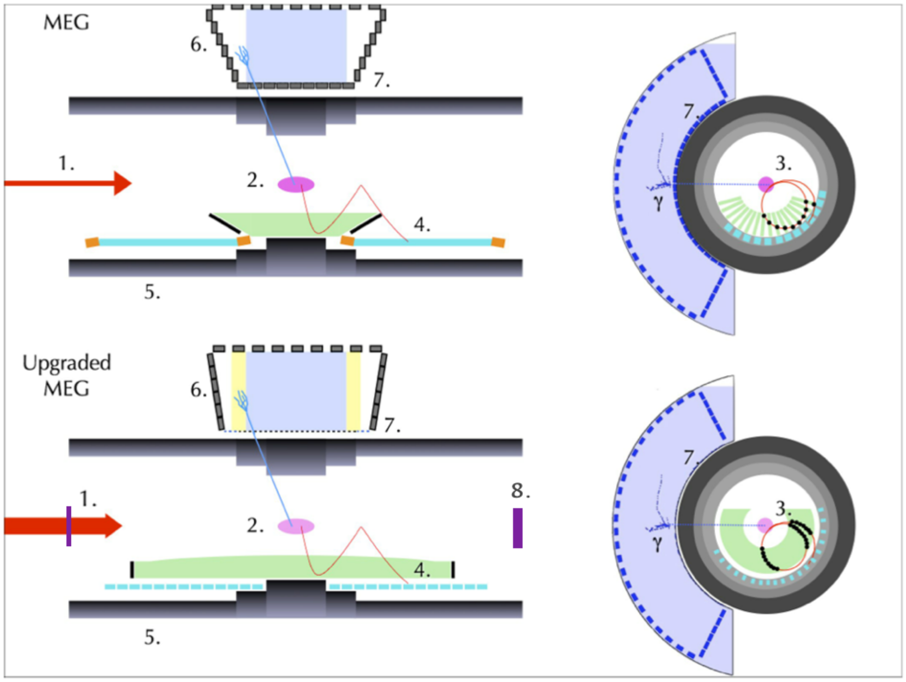

Fig. 3.25: Concept of the upgrade

Fig.3.26 illustrates the schematic view of the MEG Ⅱ experimental apparatus.

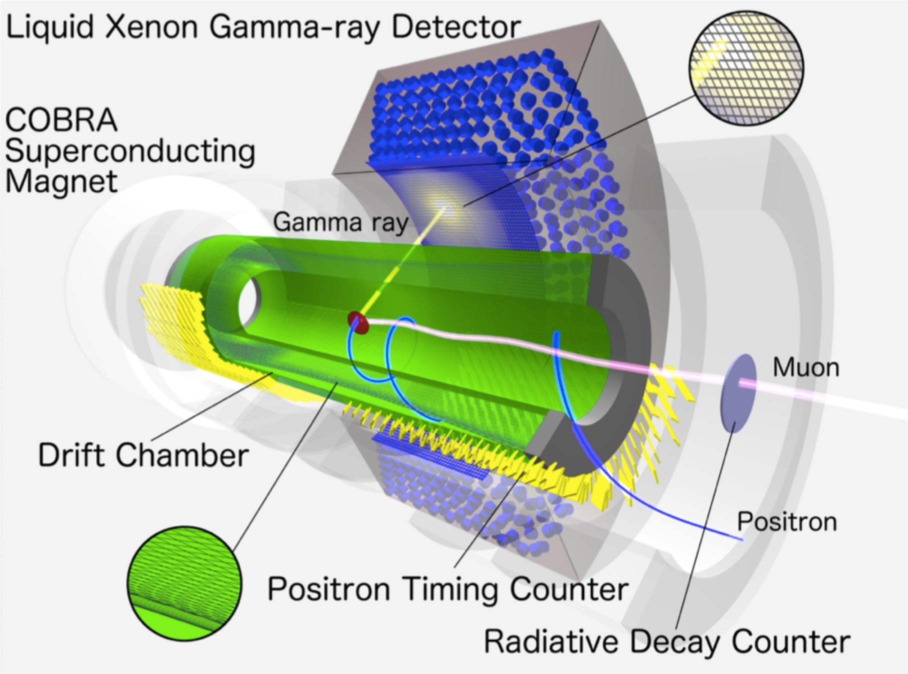

Fig. 3.26: MEG II experimental apparatus

3.2.2 μ^+ Beam and Target

A thinner target with a smaller slant angle (15°) with respect to the muon beam will be used to minimize the positron multiple scattering and the generation of the background-gamma and the muon stopping rate will be 7×10^7 muons/sec. Since there was a target deformation in the MEG experiment, the study on the target material is ongoing. The candidates are polyethylene (140 μm), beryllium (90 μm) and scintillator film (130 μm). Fig.3.27 shows MEG II muon stopping target prototype, used in the pre-engineering run 2015.

Fig. 3.27: MEG II muon stopping target prototype

3.2.3 The Positron Spectrometer

Drift chamber

The MEG II will use a completely new single volume drift chamber. It has 1200 wires with 8° stereo angles (Fig.3.28). The expected resolutions are $\sigma_{E_{e^+}}$ of 130 keV, σ_θ of 5.3 mrad and σ_ϕ of 3.7 mrad. The chamber is designed such that it is long enough for positrons not to hit massive materials and stop there before entering the timing counters. As a result, the positron efficiency will be improved from 40 % to 90 %. The mockup chamber is shown in Fig.3.29.

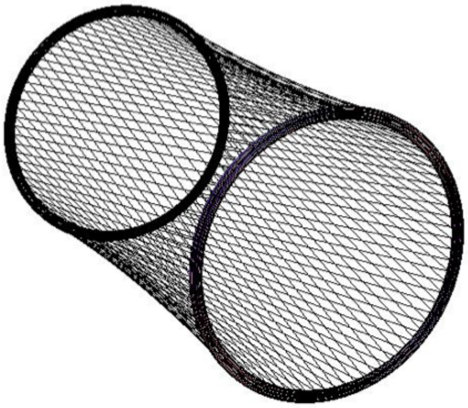

Fig. 3.28: One of the hyperbolic mesh ground planes

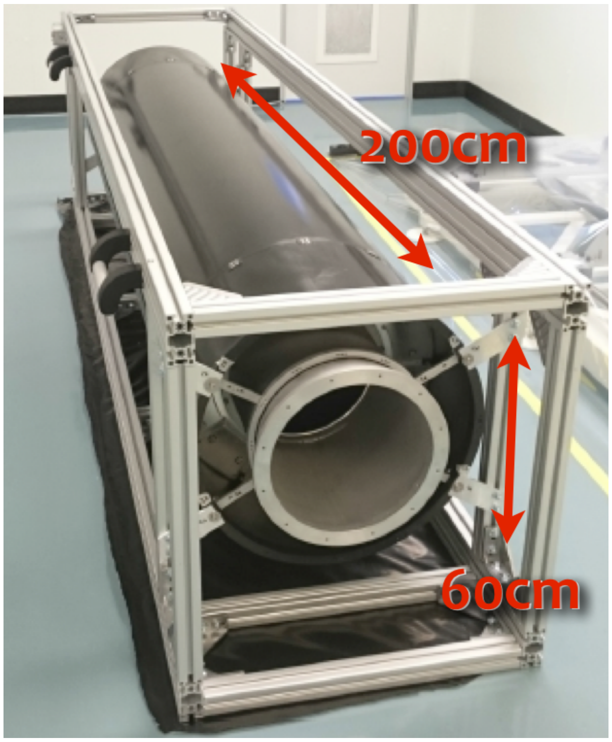

Fig. 3.29: Drift chamber mockup

Timing counter

Although the time resolution in the MEG timing counter was expected to be ~ 40 psec, a worse resolution of 65 psec was achieved because of the actual experimental conditions such as the electronics time jitter. The timing counter in the upgrade experiment consists of 512 pixelated counters with multiple SiPM readout. The time resolution of a single counter of ~ 75 psec is achieved. Fig.3.30 and Fig.3.31 are the pictures of the single counter.

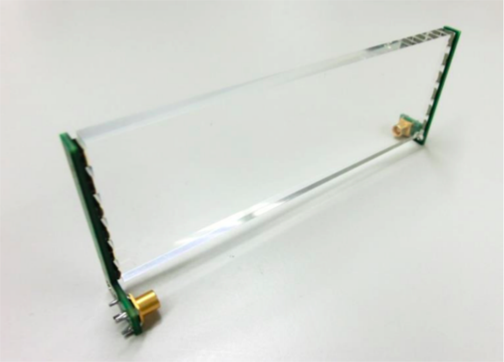

Fig. 3.30: Picture of a single counter

Fig. 3.31: Six SiPMs are series connected on a PCB and attached on both ends of a counter

A single positron hits several counters and the overall timing resolution improves depending on the number of hit counters (N_{hit}) approximately as $1/\sqrt{(N_{hit})}$. From simulations, the average N_{hit} is estimated to be about nine with the optimized counter layout. In the beam test, an excellent timing resolution of 30 psec was achieved using multiple counter hits. Fig.3.32 shows 128 counters which were being installed to the inside of the COBRA magnet.

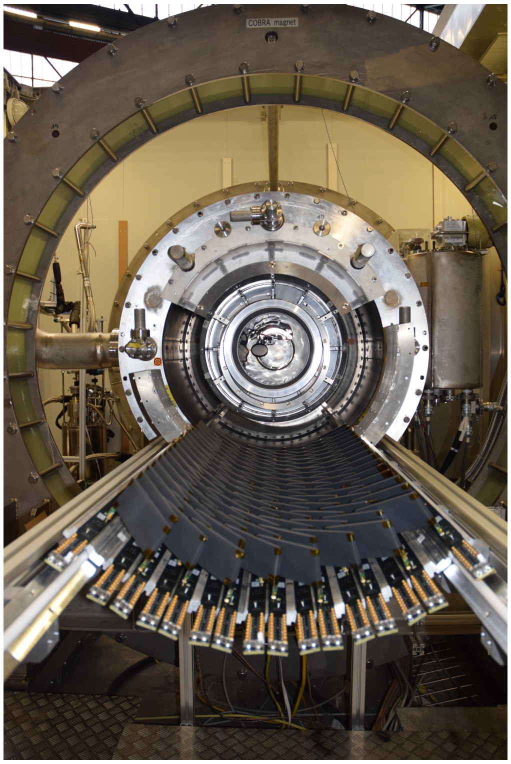

Fig. 3.32: Half of the downstream detector (128 coutners)

3.2.4 The Gamma-ray Detector

The performance of the MEG gamma ray detector is limited by the non-uniformity of photomultipliers coverage as shown in Fig.3.33. Especially the events with a shallow interaction point show bad resolutions.

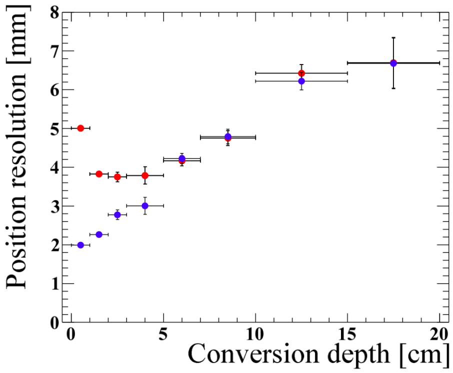

Fig. 3.33: Position resolutions as a function of the first photon conversion depth. The red markers are resolutions in the MEG experiment. The blue ones are expected resolutions in the MEG II experiment.

To improve the uniformity, 246 photomultipliers on the gamma entrance window will be replaced with 4092 SiPMs in the upgrade experiment. The number of the SiPMs are determined by the area of the gamma-ray entrance window.

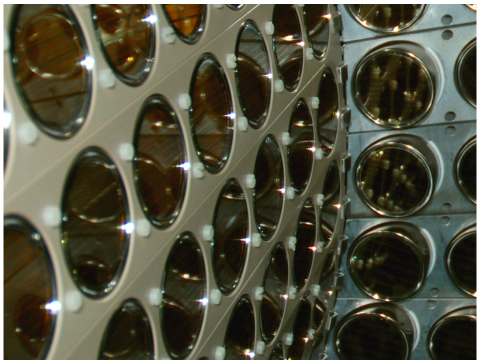

Fig. 3.34: Gamma-ray entrance window in the MEG experiment

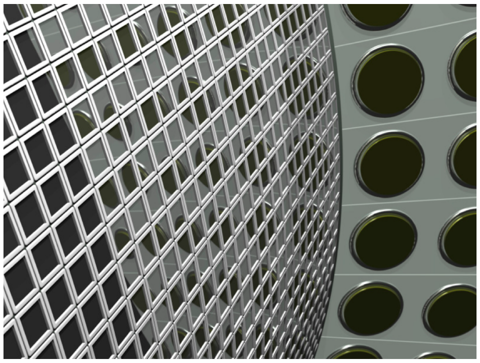

Fig. 3.35: Gamma-ray entrance window in the MEG II experiment (CG)

The MPPCs should be sensitive to the vacuum ultraviolet as the photomultipliers, and have fast responses. The MEG II collaboration and Hamamatsu Photonics have developed MPPCs which have a high photon detection efficiency (~20 %) for liquid xenon scintillation light and a fast decay time (~ 50 nsec). Fig.3.36 shows the MPPC. It has four independent sensor chips ($6{\times}6\ \mathrm{mm}^2$) and the chips are connected in series to reduce the capacitance. The basic properties of SiPMs will be given in the following chapters.

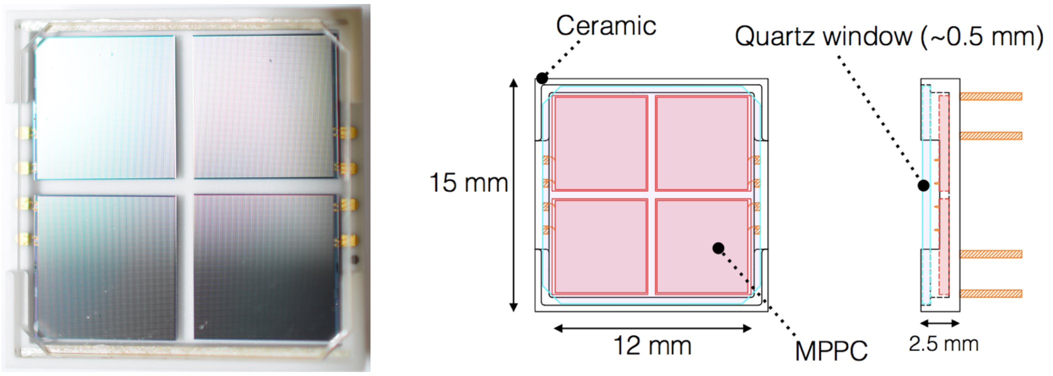

(a) Picture of the MPPC

(b) Schematic view of the MPPC

Fig. 3.36: Ultraviolet sensitive MPPC (S10943-3186)

In Fig.3.37, event displays of pileup photons in the MEG and the MEG Ⅱ gamma detector are shown. Thanks to the higher granularity of scintillation readout, the imaging power is improved and two photons are identified effectively in the upgraded detector. Accordingly, background photons from high energy positron annihilation will be reduced.

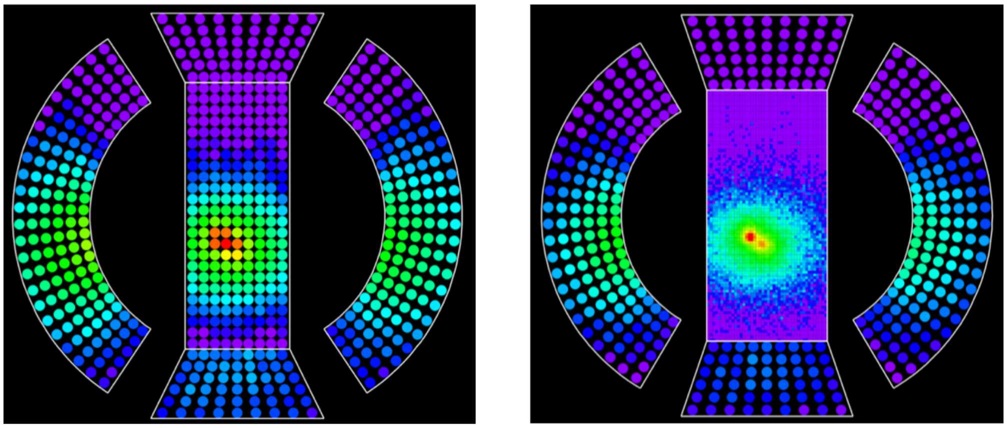

(a) Scintillation light distributions in the MEG liquid xenon detector

(b) Scintillation light distributions in the MEG II liquid xenon detector

Fig. 3.37: Collected scintillation light distribution of pileup photon events

3.2.5 Background Tagging Detector

In the MEG II experiment, a new detector for active background tagging will be introduced. The details are discussed in the next chapter.

3.2.6 New DAQ board

The MEG II experiment needs more DAQ and trigger channels. In addition to the space problem, the new drift chamber adopts the timing technique which requires the higher bandwidth. To fulfill the requirements, a new DAQ board called WaveDREAM was proposed.

The basic idea of the WaveDREAM is to merge the waveform digitizing technology with the trigger while improving the bandwidth. To realize the better bandwidth, a new front-end was designed and tested as can be seen in Fig.3.38, Fig.3.39 and Fig.3.40. In addition to them, the SiPM power supply is also included in the WaveDREAM.

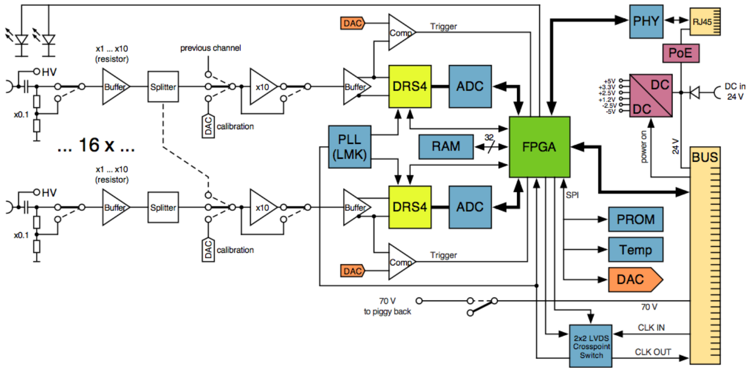

Fig. 3.38: Simplified scheme of the DAQ board

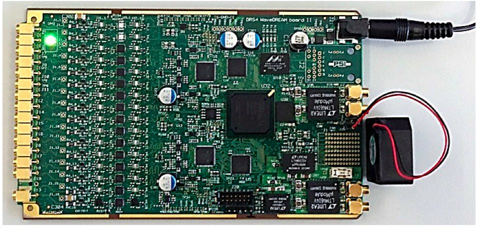

Fig. 3.39: The WaveDREAM board

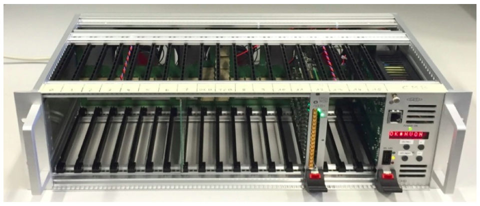

Fig. 3.40: Crate to place the WaveDREAM board

Chapter 4

Radiative Decay Counter (RDC)

The MEG Ⅱ experiment will use a twice μ^+ beam rate and the influence of the accidental background will be more serious. To further improve the ultimate sensitivity of MEG Ⅱ, we will introduce a new detector, the "Radiative Decay Counter (RDC)", which actively tags the accidental background events. The basic idea and the detector design will be discussed in this chapter.

4.1 Mechanism of background identification

As explained before, the dominant background in $\mu^+ \to e^+\gamma$ search are the accidental background. The background gamma-ray mainly comes from a Radiative Muon Decay (RMD: $\mu^+ \to e^+\nu_e\overline{\nu}_\mu\gamma$) or a positron Annihilation In Flight (AIF) as can be seen in Fig.4.1. The rate of the AIF gets smaller thanks to the low mass tracker in the MEG Ⅱ. However, the amount of the gamma-ray from the RMD will not benefit from the improved detector because the amount of background gamma-rays is determined by the branching fraction of RMD. Therefore, an active identification of background gamma rays from RMD is needed to further improve the experiment's sensitivity.

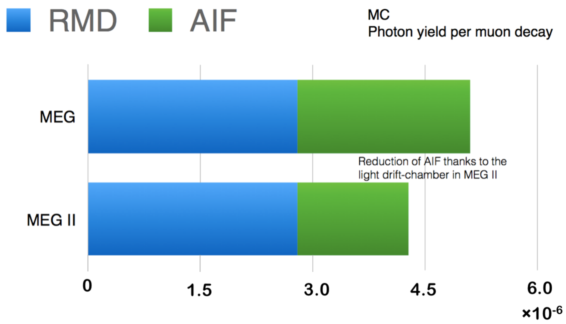

Fig. 4.1: The amount of background gamma rays (E_γ> 48 MeV) in the MEG experiment and the MEG Ⅱ experiment.

When a high energy gamma ray (> 48 MeV) is emitted from an RMD, a low momentum positron (2-5 MeV typically) is emitted with a high probability. Such low momentum positrons have a so small bending radius that they are out of the acceptance of the MEG tracker. By installing a new positron detector, RDC, on the central axis of the solenoid, an identification of background gamma rays from RMDs is possible (Fig.4.2 and Fig.4.3). The RDC will identify 54 % of the total background gamma rays and will improve the sensitivity by 28 %.

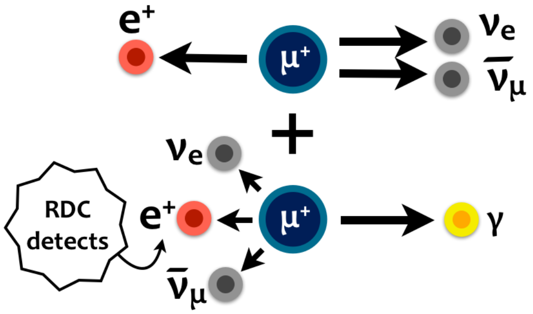

Fig. 4.2: An example of a background event identified by RDC

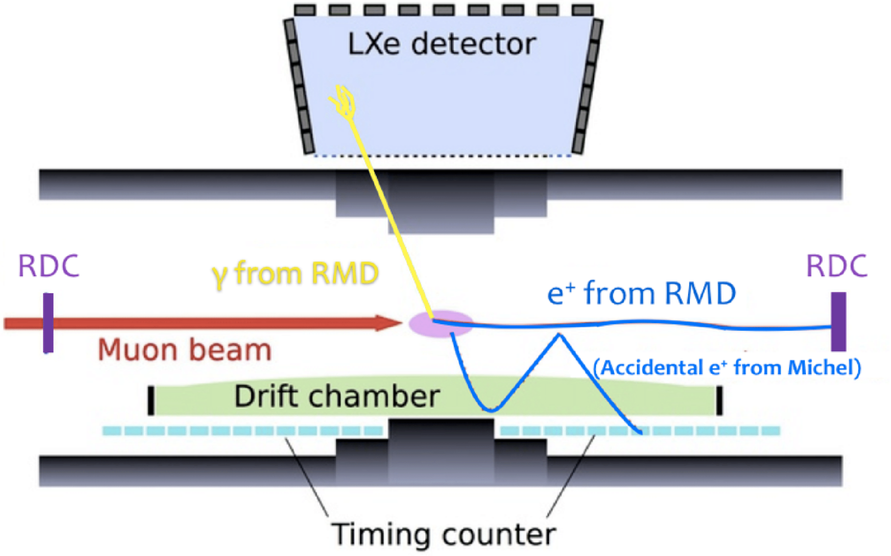

Fig. 4.3: Concept of the RDC

The RDC measures the positron hit time by plastic scintillation detectors with a fast response and checks time coincidence with the gamma ray measured in the liquid Xenon detector. As can be seen in Fig.4.4, the time difference between the positron's hit in the RDC and the gamma-ray's hit in the liquid Xenon detector has a peak with a FWHM of ~ 6 nsec due to the positron's time-of-flight from the muon stopping target to the RDC. Therefore, the time resolution of 100 psec which has already been obtained in the lab test is enough for the RMD detection.

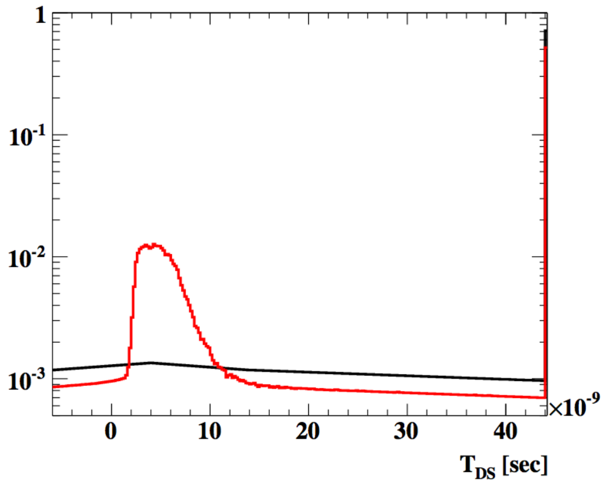

Fig. 4.4: The time difference between the positron's hit in the downstream RDC and the gamma-ray's hit in the liquid Xenon detector (red line). The time resolution of 100 psec is included. The black line is the accidental positron hit from Michel decay.

In addition to the hit time, the downstream RDC will be able to measure the energy deposit. Positrons which hit the RDC come not only from RMD but also from Michel decay. The positrons from Michel decay have a larger momentum (Fig.4.5). Hence, the signal-to-background ratio in the RMD-tagging is improved by measuring the positron energy deposit.

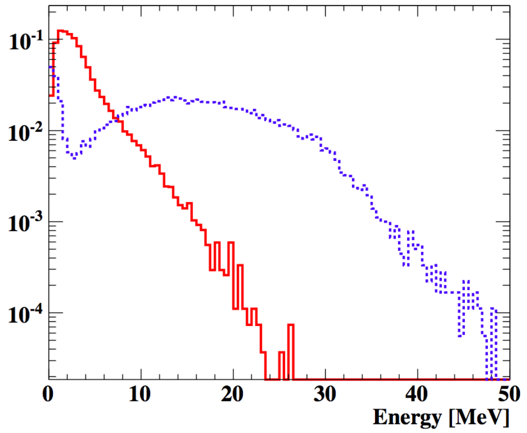

Fig. 4.5: Energy deposit in the downstream RDC. Blue: positrons from Michel decay. Red: positrons from RMD with > 48 MeV energy gamma ray.

4.2 Simulation Study on Sensitivity Improvement

The sensitivity dependent on the time and energy resolutions of the RDC was estimated. Here, the experiment sensitivity is defined as the median upper limit of an ensemble of pseudo experiments with the background-only hypothesis. Fig.4.6 illustrates the distribution of N_{sig} upper limit at 90 % C.L. where N_{sig} is the number of signal events.

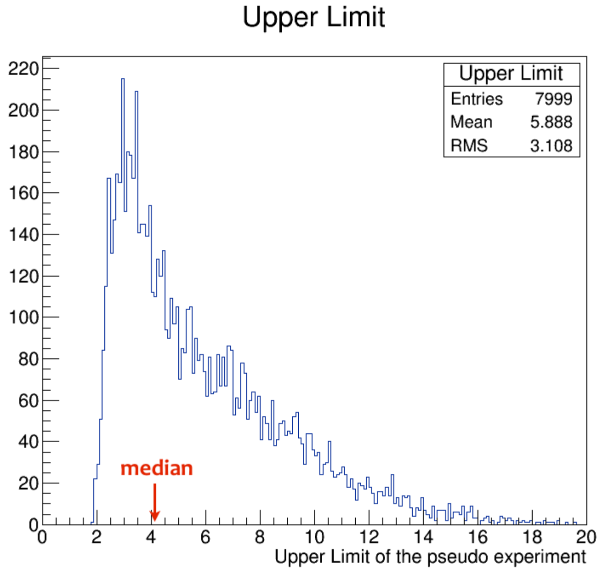

Fig. 4.6: Distribution of the upper limit of the 7999 pseudo experiments. The time resolution of the upstream, the one of the downstream, and the energy resolution are assumed to be 500 psec, 100 psec, and 8 % respectively.

The downstream RDC with the time resolution of 100 psec and the energy resolution of 8 % improves the sensitivity by 16 %. Fig.4.7 shows the expected sensitivity as a function of the RDC downstream resolution. The improvement due to the upstream RDC which has the time resolutions of 500 psec is included. As can be seen in the figures, the sensitivity is flat around time resolution of 100 psec or the energy resolution of 8 % which were already obtained in the lab test.

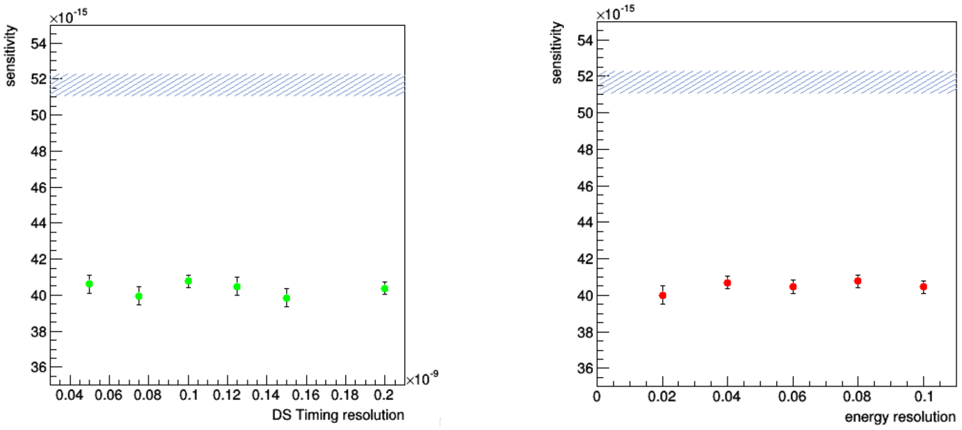

(a) Sensitivity as a function of the time resolution of the downstream RDC

(b) Sensitivity as a function of the energy resolution of the downstream RDC

Fig. 4.7: The sensitivity as a function of the downstream RDC performance. The blue bands are the sensitivity of the MEG II experiment without the RDC

4.3 Detector Design

Since the RDC will be set on the central axis of the solenoid (or the μ^+ beam axis), it should satisfy these requirements:

- compact enough to be placed in the limited space
- operational in the magnetic field
- cope with MHz order positron hits
- a high efficiency
- does not generate background gamma rays

To meet the first and the second requirement, SiPMs are used for scintillation light collection because they are compact and not affected by magnetic fields.

The RDC consists of the beam upstream and downstream parts. The detector radius is about 9 cm, which is large enough to detect most of the low momentum positrons from RMD when the associated γ-ray has an energy above 48 MeV. The upstream and downstream parts will be placed on both COBRA endcaps (Fig.4.8).

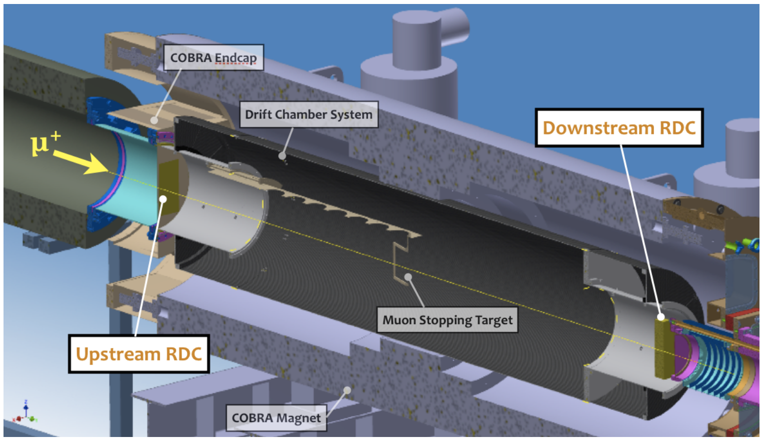

Fig. 4.8: Schematic view of MEG II detector with the full RDC. The RDC detectors are placed inside both COBRA endcaps.

4.3.1 Upstream RDC

To minimize the effect on the μ^+ transport, the upstream detector is designed to be thin. It is made of 704 squared scintillation fibers with 250 μm thickness as shown in Fig.4.9.

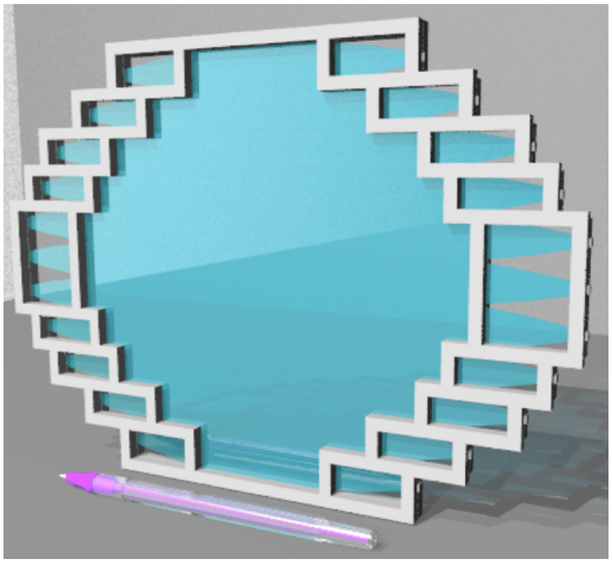

Fig. 4.9: Upstream RDC design

The scintillation fibers will be glued for the detector to be flat and they will be bundled at both ends and read out by SiPMs.

For the prototype, fibers with a thickness of 265-270 μm were glued (Fig.4.10). A plastic mylar film with 12 μm thickness will be attached as support structure.

The inefficiency of the detector, which will affect the RMD performance, is caused by the SiPM recovery time, the fiber clad and the low light yield of the fiber. For example, the inefficiency due to the recovery time of 50 nsec can be estimated to be about 3 % for the individual fiber placed around the center where the hit rate is 0.6 MHz. The detailed study of these effects is ongoing.

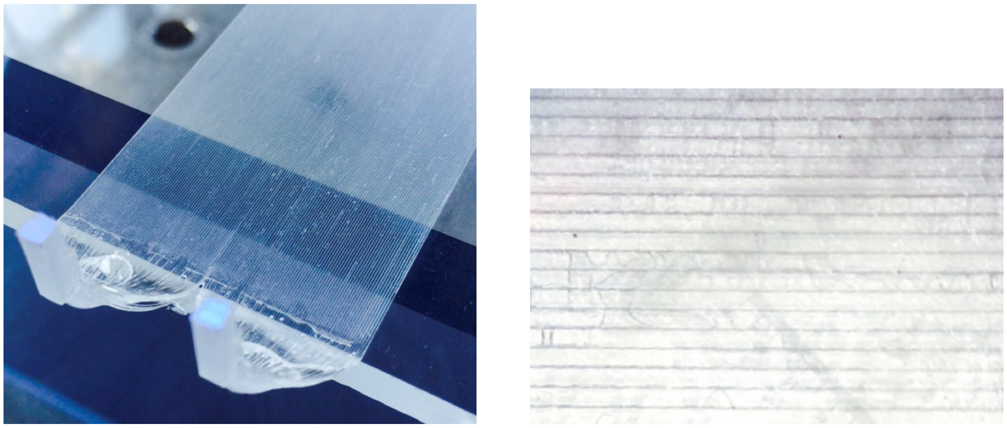

(a) 64 fibers are bundled and bent by 90 degrees due to space limitation.

(b) Picture of the glued fiber surface taken with a microscope

Fig. 4.10: Upstream RDC prototype

4.3.2 Downstream RDC

Since the downstream detector has nothing to do with the muon beam transportation, a more massive detector can be mounted in the downstream part. The downstream RDC consists of 12 plastic scintillator bars for the hit time measurement and 76 LYSO crystals for the energy deposit observation (Fig.4.11 and Fig.4.12). The plastic scintillator bars have a thickness of 5 mm and the their length ranges from 7 to 19 cm. The width of the bars is 1 or 2 cm. The bars placed near the beam axis have the smaller width to cope with the high hit rate. The size of the LYSO crystal is 2×2×2 cm^3. MPPCs are used for the scintillation light readout.

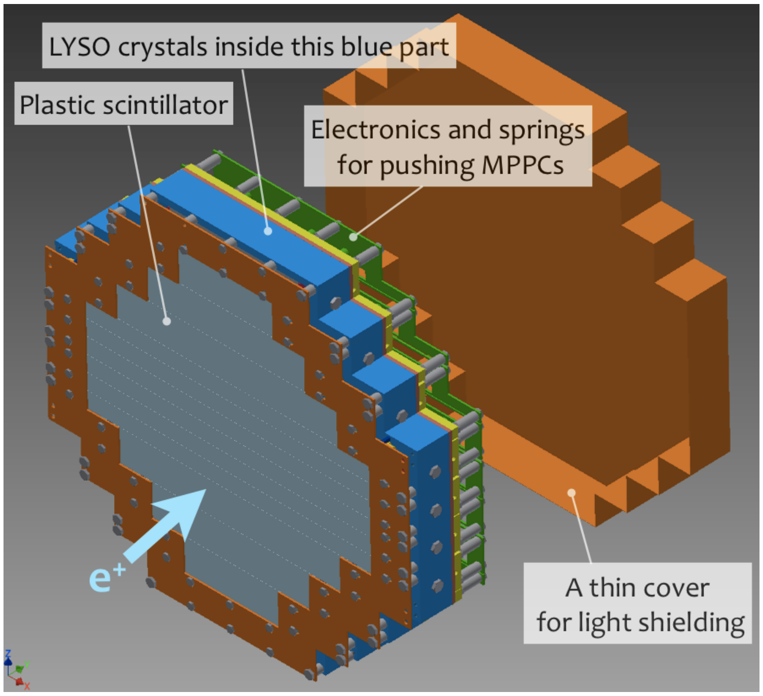

Fig. 4.11: Downstream RDC design

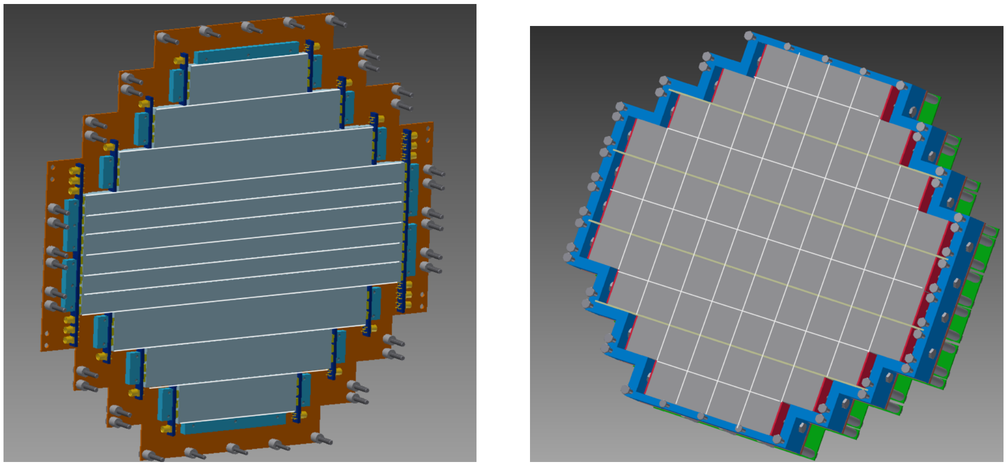

(a) Plastic scintillator counters

(b) LYSO counters

Fig. 4.12: (a) Timing Counter part and (b) Calorimeter Part of the Downstream RDC

4.4 Beam Test with a Prototype

4.4.1 Downstream part

We demonstrated in a beam test using a prototype detector that RMD events can be identified by the RDC. A clear RMD time peak was observed in the RDC-liquid xenon coincidence trigger. After getting the results, the installation of the downstream part was approved by the MEG II collaboration and the construction has started.

4.4.2 Upstream part

The effect on the beam properties due to the upstream RDC was simulated. The muon stopping efficiency is decreased by 3 % (from 71.9 % to 69.8 %) with the RDC. With regards to the beam spread, sigma X increases by 7 % (from 1.11 cm to 1.19 cm) and sigma Y by 5.9 % (from 1.07 cm to 1.13 cm).

The investigation of the effect with the muon beam using a mockup detector is still ongoing and the MEG II collaboration will decide whether it should be accepted or not based on the result. Preliminary results show that the effects on the beam are small.

Chapter 5

Downstream Counter Optimization

5.1 Scintillator Selection

Since the RDC is placed on the μ^+ beam axis and the emitted positrons spiral out in the beam axis direction due to the COBRA magnet, the positron hit rate in the RDC is high. The detector should be optimized to have a fast response to cope with the positron rate.

5.1.1 Plastic Scintillator

Plastic scintillators are the most widely used particle detection device. They have an excellently fast response of O(nsec) and are suitable for the timing counter devices. For small-size scintillators, BC-418 and BC-422 from Saint-Gobain (Table 5.1) are the best candidates.

Table 5.1: Basic Properties of BC-418 & BC-422 [15]

	BC-418	BC-422
Light Output, %Anthracene	67	55
Rise Time, (ns)	0.5	0.35
Decay Time (ns)	1.4	1.6
Pulse width, FWHM, (ns)	1.2	1.3
Wavelength of Max. Emission, nm	391	370

The time resolution of the small plastic scintillators largely depends on the number of detected photons. In addition to the light yield, the detection efficiency for the scintillation light is also important. MPPCs, used for readout as will be described later, have a peak in the detection efficiency around 450 nm (Fig.5.2), so BC-418 is advantageous as can be seen in Table 5.1 and Fig.5.1.

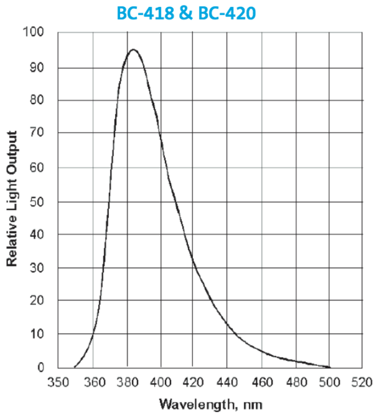

Fig. 5.1: Emission spectrum of BC-418 & BC-420 [15]

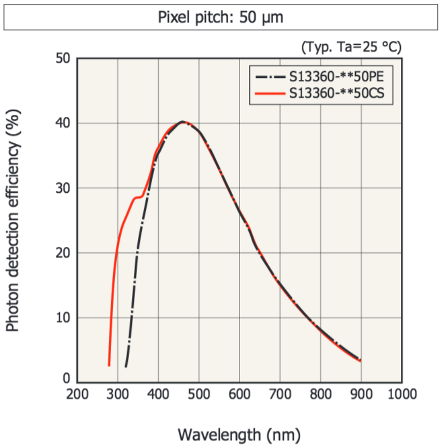

Fig. 5.2: Photon detection efficiency vs wavelength for S13360 series MPPC [23]

Considering the properties, we decided to use BC-418 for the RDC timing counter part.

5.1.2 Inorganic Scintillator

In order to achieve a good energy resolution, high photon statistics are necessary. For the RDC detector calorimeter part, the scintillator should have a fast decay time to reduce pileup events. From these points of view, GSO and LYSO are good candidates. Table. 5.2 shows basic properties on various inorganic scintillators.

Table 5.2: Inorganic Scintillator Properties

Inorganic scintillator	NaI	BGO	LSO	GSO	LYSO
Density (g/cm^3)	3.67	7.13	7.40	6.71	7.1
Attenuation length (cm)	2.6	1.11	1.14	1.38	1.12
Decay time (ns)	230	300	40	30-60	41
Wave length (nm)	415	480	420	430	420
Relative light yield	100	7-12	40-75	20	70-80

5.1.3 Self-radiation as energy calibration source

Lutetium yttrium orthosilicate (LYSO) contains the radioactive isotope ^{176}Lu. The abundance of ^{176}Lu in Lutetium is 2.6 % and it has a long life time of 3.6×10^{10} years as can be seen in Fig.5.3. We measured the rate of the self-radiation with a prototype detector and checked if it can be used for the energy calibration. The setup is the following Fig.5.5:

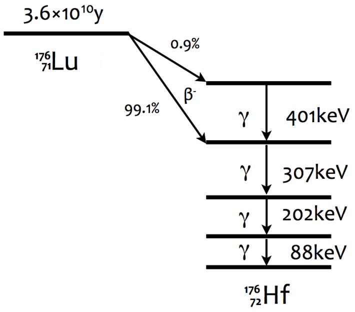

Fig. 5.3: Decay scheme of ^{176}Lu to ^{176}Hf

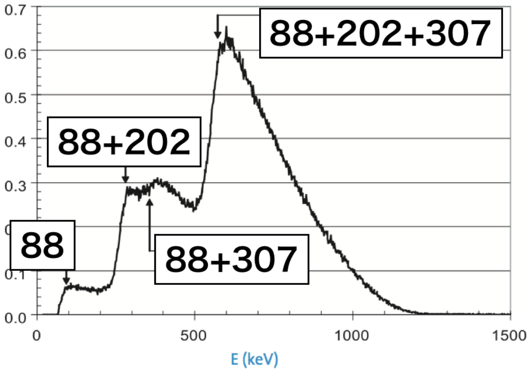

Fig. 5.4: The energy spectrum of LYSO self-radiation [20]

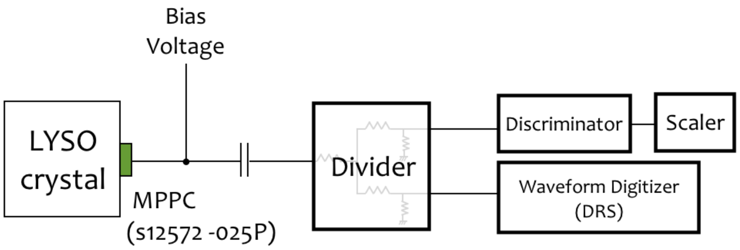

Fig. 5.5: Setup for LYSO self-radiation rate measurement

The rate was measured with a scaler. In parallel, waveforms were aquired with the DRS to know the energy. The discriminator and the DRS have a common threshold level. The measured rate was 2.1 kHz for energies > 250 keV as shown in Fig.5.6. The rate is large enough for the self-radiation to be used as calibration source.

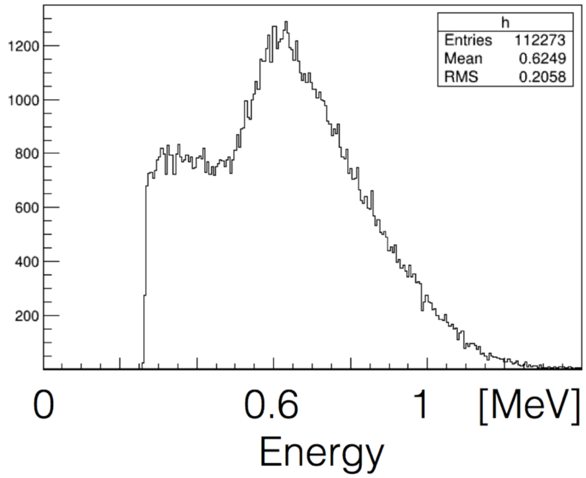

Fig. 5.6: Measured energy spectrum of the LYSO self-radiation

On the other hand, the self-radiation can be a background source through the accidental pileup. Here we consider the pileup ratio due to the self-radiation. Assuming that the pulse length ΔT is 500 nsec, the fraction of the pileup events due to the self-radiation f_{self} = 2kHz is roughly estimated to be:

$$2 \times \Delta T \times f_{self} = 10^{-3} \tag{5.1}$$

This small value will not affect the performance significantly. Considering the result and the high light yield, we decided to use LYSO.

5.2 SiPM Selection

One type of popular photon sensitive devices in particle physics experiments is Silicon Photomultipliers (SiPM). SiPMs have several advantages:

- high photon detection efficiency
- high gain
- good time resolution
- compact

- insensitive to magnetic fields

For the RDC construction, Multi-Pixel Photon Counters (MPPCs) developed by HAMAMATSU Photonics are used. We have studied several MPPC models and optimized the RDC. In this section basic properties of the SiPMs are described first and the optimization process will be discussed.

5.2.1 Basic Properties of SiPMs

A SiPM is a multi-pixelated avalanche photodiode operating in "Geiger mode". The Geiger mode is a condition where the reverse voltage applied on a SiPM is higher than the breakdown voltage and even weak light can cause a discharge.

The basic idea of SiPMs is to precisely count the number of incoming photons.

Structure & Principle

If an incident photon is absorbed, an electron-hole pair is generated (Fig.5.7 and Fig.5.8). The electron drifts in the depletion layer and is accelerated by a high electric field of $O(10^5)$ V/cm. The electron acquires sufficient energy to produce further electron-hole pairs through impact ionization and triggers the avalanche. This avalanche stops when the current flows through the resistor which is attached on each cell ("pixel") and the voltage drops below the breakdown voltage.

Photon Detection Efficiency

The absorption of incident photons and the generation of photoelectrons are important processes since they determine the photon detector efficiency. It is expressed as Photon Detection Efficiency (PDE) and the PDE is defined as

$$PDF = \epsilon \times QE \times P_{trigger} \tag{5.2}$$

where ϵ is the fill factor (the fraction of the active area), QE is the quantum efficiency (probability for the photon entering the active area to create a electron-hole pair) and $P_{trigger}$ is the probability for the carrier to trigger avalanche.

Gain

Thanks to the avalanche process of the carrier in the electric field, the amount of pulse charge is large enough to be measured. The degree of the multiplication is expressed as the gain. The gain is defined as

$$G = \frac{Q}{e} \tag{5.3}$$

where Q is the pulse charge and e is the elementary charge. The gain is roughly proportional the pixel size which corresponds to the capacitance of each cell.

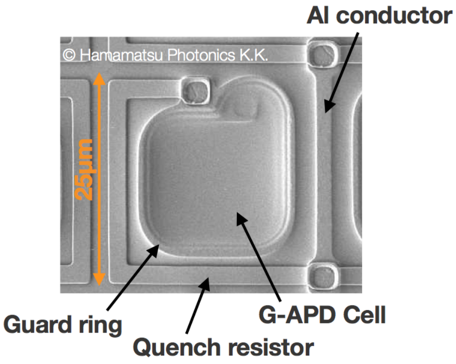

Fig. 5.7: Surface of the SiPM

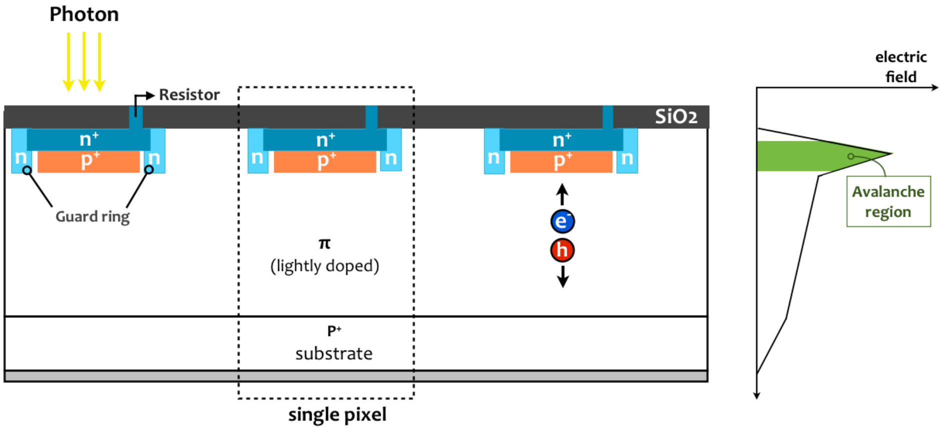

Fig. 5.8: SiPM structure

Crosstalk and After-pulsing

A triggered pixel can induce an avalanche in neighboring pixels and this phenomenon is called crosstalk. A carrier from the primary avalanche can be trapped and released after quenching. Since this delayed release can trigger another avalanche, it is called after-pulsing. These parasitic avalanches are the limitation factor the SiPM performance.

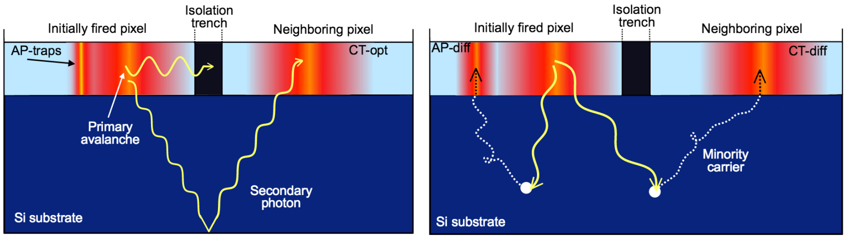

(a) (b)

Fig. 5.9: Conceptual picture of the crosstalk and the after-pulse [21]

5.2.2 Energy Resolution

To distinguish the RMD positron from the Michel decay positron, a calorimeter with a good energy resolution is needed. While the energy resolution is determined mainly by the crystal light yield, the properties of photon sensors can also affect the performance. The overvoltage dependence of the energy resolution was studied for four types of MPPCs [22] as shown in Table. 5.3.

Table 5.3: Four types of MPPC used for the test. They have a 3×3 mm^2 active area

MPPC type	pixel size μm	number of pixels	fill factor %	CT suppress
S12572-015P	15	40000	53	without
S12572-025P	25	14400	65	without
S12572-050P	50	3600	62	without
S13360-3050PE	50	3600	74	with

For the study, ^{60}Co is used as a gamma source and an MPPC is attached to a LYSO crystal whose size is $2\times2\times2$ cm^3. Optical grease is used for the coupling. The data is acquired by self-triggered condition and contains the effect of the ^{176}Lu decay (see Fig.5.1.3).

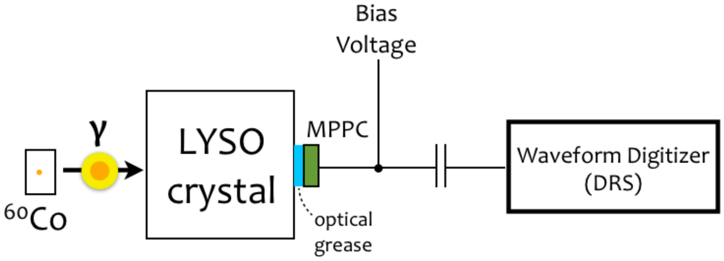

Fig. 5.10: Setup to measure the energy resolution

In Fig.5.11, an example of the observed energy spectrum is shown. The photo-peaks are fitted with gaussians. Here we define the energy resolution R as

$$R = \frac{\sigma}{E_\gamma} \tag{5.4}$$

where E_γ and σ are the mean and the width of the photo-peak respectively.

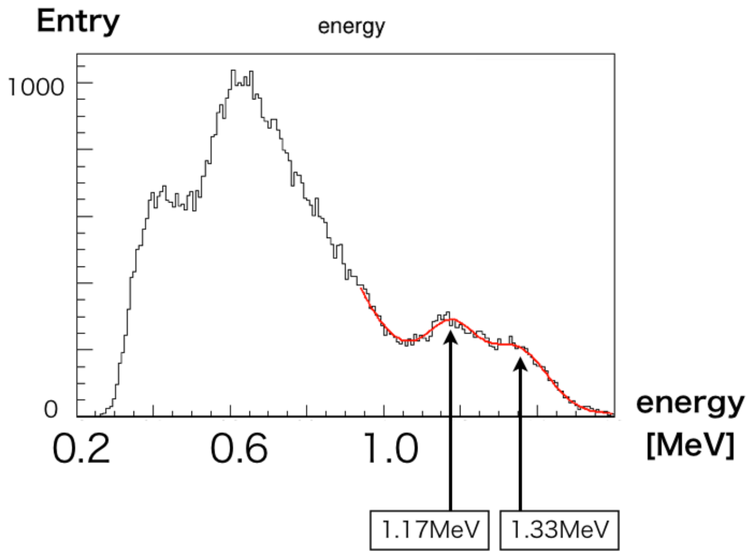

Fig. 5.11: Observed ^{60}Co and self-radiation energy spectrum. The two photo-peaks at 1.17 MeV and 1.33 MeV are fitted with gaussian functions. The background floor is fitted with an exponential function.

The measured energy resolution for each kind of MPPC is shown in Fig.5.12. As the applied voltage increases, the energy resolution gets better thanks to the higher PDE. However, the optical crosstalk probability also gets large at high over-voltage and it limits the improvement due to the fluctuation of the number of the fired pixels.

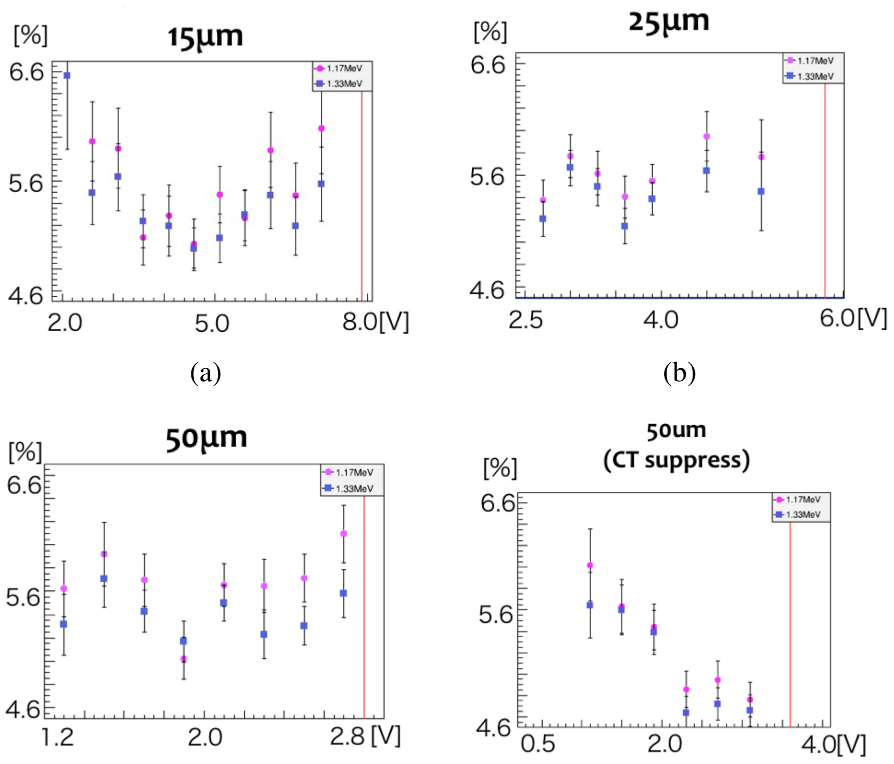

(a) (b)

(c) (d)

Fig. 5.12: Energy resolution as a function of the overvoltage for four types of MPPCs

The required energy resolution is 8 % at 1 MeV and all four types of MPPCs satisfy the condition. We have chosen the MPPC considering other factors.

S12572-050P and S13360-3050PE have the largest pixel size and the waveform for high energy particles can be deformed due to the saturation of the pixels. The deformation can make it difficult to separate piled up pulses by waveform analysis. S12572-015P has the smallest gain due to the pixel size and shows the worst signal-to-noise ratio. This can be a problem when the MPPC accumulates radiation damage and the noise level gets worse.

Therefore, S12572-025P has a good balance and we decided to use this type for the calorimeter part.

5.3 Estimation of the Current through the MPPC

For the HV power supply, the current limit is one of the important factors to determine the operation range. While the current limit of the HV power supply for the MEG II experiment is 100 μA by default, the RDC requires a larger current limit due to the high positron hit rate. Therefore, the estimation of the current through the MPPCs is necessary.

First, the positron average energy deposit and hit rate for all crystals were estimated by a simulation. Fig.5.13 shows the energy deposit per seconds in the crystals.

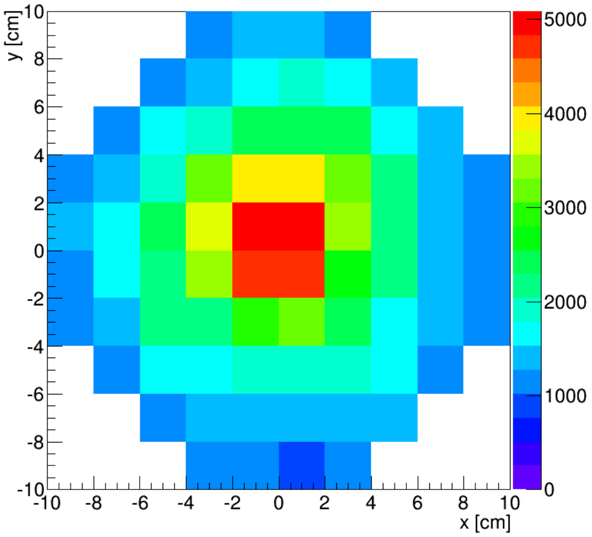

Fig. 5.13: Average positron energy deposit times hit rate in each crystal [GeV/sec]

The energy deposit in the crystals around beam axis is large (~5 TeV/sec) because of the MHz order hit rate.

Second, the charge value at the 1.13 MeV photo-peak of ^{60}Co measured with an MPPC coupled to a LYSO crystal was calculated (Fig.5.14). The current for each crystal was estimated as (the charge) / (1.13 MeV) × (mean energy deposit) × (hit rate). The current ranges from 80 μA to 400 μA. The overvoltage is set to about 5 V which is larger than the actual operation voltage and the current should be smaller than in this test's result.

Third, as a cross check, we measured the current increase due to exposure to ^{90}Sr and the corresponding hit rate (Fig.5.15). The voltage is supplied and the current is measured by a picoammeter. From the dose ratio of measured and simulated hits, the current in the actual run is estimated to be 80 μA to 400 μA and is consistent with the ^{60}Co result.

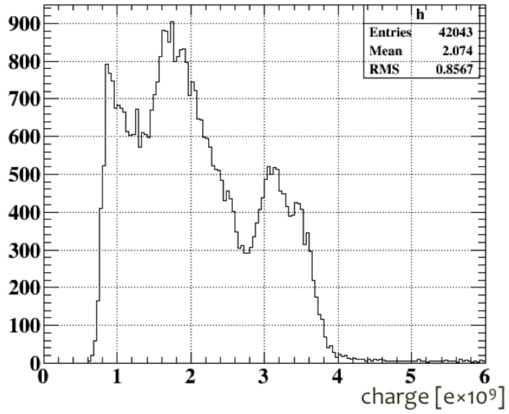

Fig. 5.14: Charge distribution of ^{60}Co and the self-radiation from LYSO.

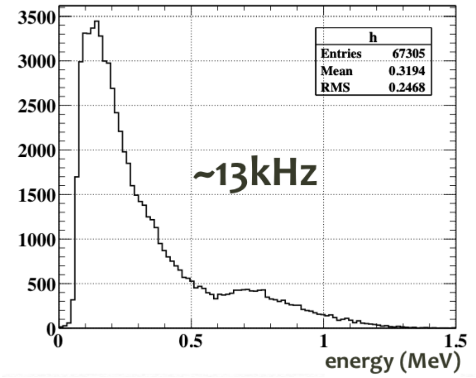

Fig. 5.15: Measured spectrum of the radiation from ^{90}Sr

As a result, the HV power supply for the RDC should reach 1 mA instead of 100 μA and it will be developed to meet this requirement.

5.3.1 Afterglow

When testing the crystal properties, the current through the attached MPPC significantly fluctuated for some crystals and it seemed that weak light from the crystal reached the MPPC even if it was not exposed to a radioactive source (Fig.5.16). Also, the current increased after leaving the crystal in room light. After exposing the crystal to the room light over 10 hours, we measured the current as a function of time for the crystal with the highest current and it showed an exponential decay with a time constant of ~ 90 minutes (Fig.5.17). It turned out that it was caused by an afterglow of LYSO crystal. The aferglow may affect the detector's performance such as the energy resolution due to the photon number fluctuation and we are currently studying the effect.

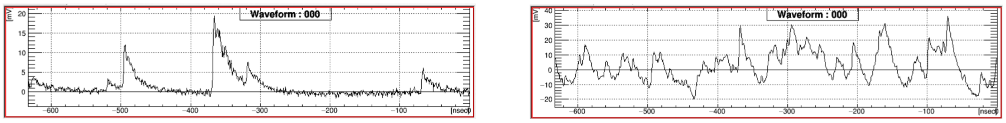

(a) (b)

Fig. 5.16: Waveforms of photons (a) from the crystal with small afterglow and (b) from the crystal with large afterglow. The significant number of photons were observed even if the crystals were not exposed to the radioactive source.

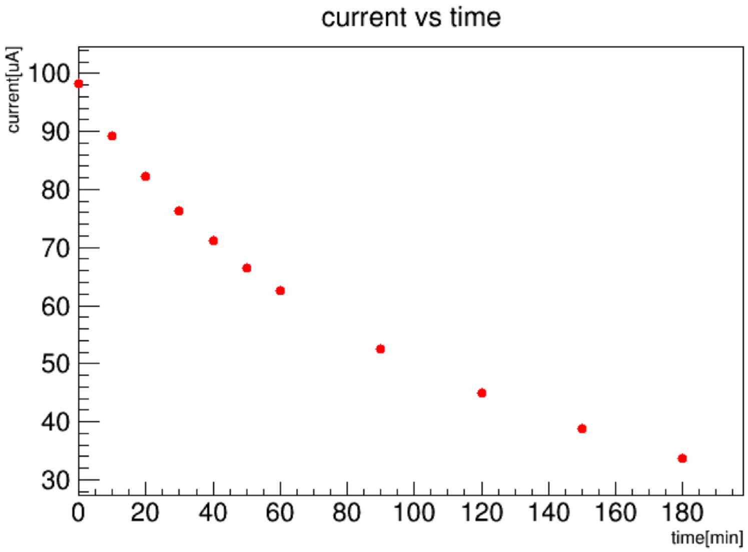

Fig. 5.17: The current through the MPPC attached to the LYSO crystal with the largest afterglow was monitored for 3 hours with a Picoammeter, after exposing the crystal to the room light over 10 hours. The light-shielding started at time= 0. The overvoltage applied to the MPPC was about 4 V.

5.4 MPPC Grouping for the Plastic Scintillators

Since the light yield of plastic scintillators is small, the gain of the attached MPPCs should be large to obtain the sufficiently good signal-to-noise ratio. Therefore, the type of S13360-3050PE which has a 50×50 μm^2 pixel size and a 3×3 mm^2 sensor area with the crosstalk suppression was chosen for the plastic scintillators.

In addition to the area covered by the attached MPPCs, the connection of the MPPCs also affects the counter performance because the pulse shape, especially the tail, depends on the sensor capacitance. In order to realize a good time resolution, the series connection is the best way because of the smallest capacitance. Fig.5.18 illustrates the model circuit of the SiPMs connected in series where only one pixel is activated, the bias circuit for the SiPMs and a signal amplifier circuit. As can be seen in Fig.5.19, the signal waveform of the series-connected SiPMs gets sharper than the waveform of the single SiPM.

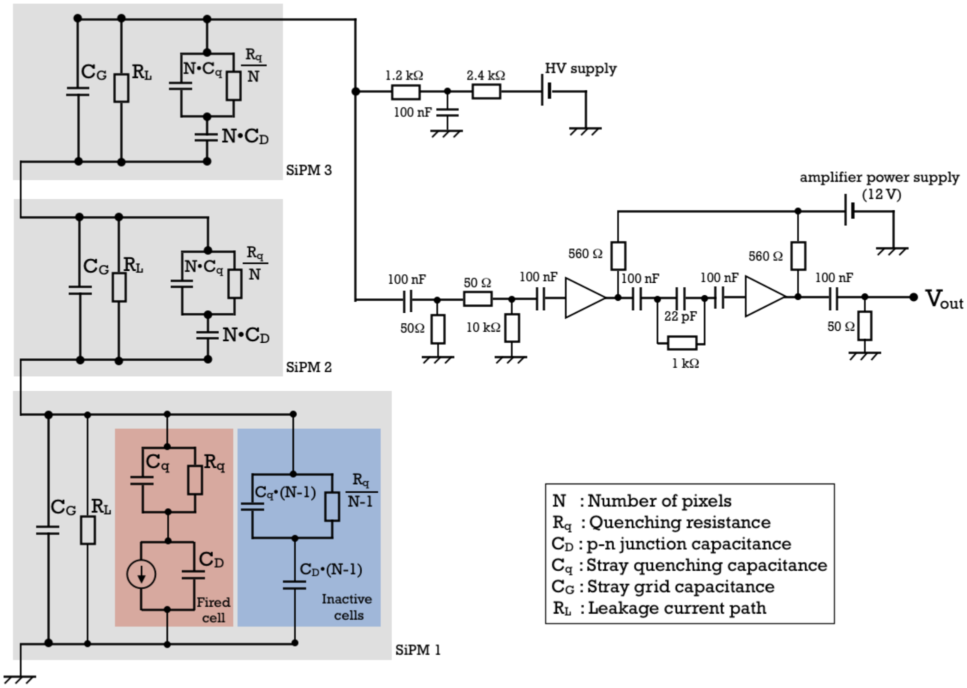

Fig. 5.18: Circuit model of series-connected SiPMs. Each gray area illustrates each SiPM. The red and the blue regions correspond to a fired pixel and inactive pixels respectively, that is, only one pixel in SiPM1 is fired in this figure.

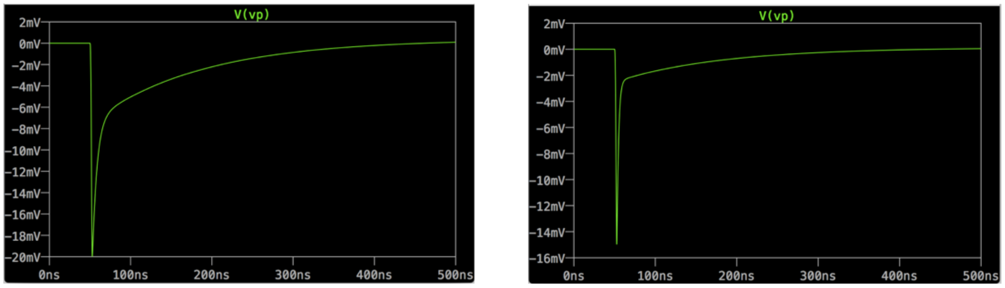

(a) (b)

Fig. 5.19: Single photon waveforms simulated with SPICE (Simulation Program with Integrated Circuit Emphasis). (a) only one SiPM is placed in the circuit. (b) three SiPMs are connected in series as shown in Fig.5.18. This simulation was conducted by Kohei Yoshida with parameters of AdvanSiD [26] which is one type of SiPMs.

For the proper operation of the series-connected MPPCs, the MPPCs in the same connection should have similar properties. Especially the shape of the I-V curve should be the same for all MPPCs in series. In order to group the MPPCs, the I-V curves of all of MPPCs were measured as can be seen in Fig5.20 and 5.21. Since the current through the MPPCs are common in the series connected circuit, the overvoltages for the MPPCs which have similar shapes of the I-V curve are automatically adjusted to the same values. Hence, the MPPCs with similar I-V curves are selected to be used in the same connection.

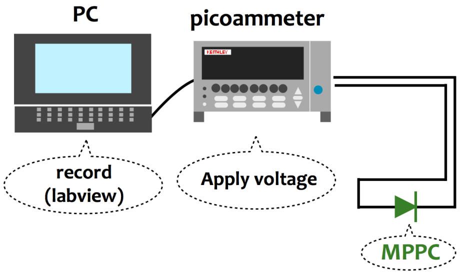

Fig. 5.20: Setup for the I-V curve measurement.

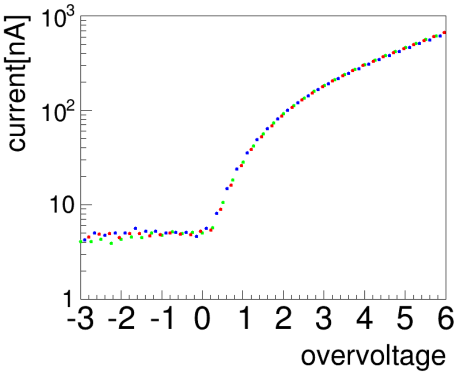

Fig. 5.21: I-V curves of three MPPCs in the same group. The plot of different MPPCs is drawn in different colors.

To measure the I-V curve, the applied voltage ranges from 48 V to 62 V in steps of 0.25 V. The current through the MPPC is automatically measured using a picoammeter with a labview software program. To reduce the fluctuation, the current is obtained 30 times at each voltage point and the corresponding average is used as the representative. The temperature is controlled by a thermostat chamber.

The overvoltage applied to the MPPCs for the operation will be about 2.5 V. The MPPCs were sorted according to the current at 2.5 V and the MPPCs were grouped according to the order obtained by the sorting procedure.

Chapter 6

Counter Construction

Since the MEG II experiment aims at starting data taking in 2016, completing the detectors is one of the most important tasks. As mentioned above, the installation of the downstream RDC was approved by the MEG collaboration and the production has started. In this chapter, the construction of the plastic scintillator and the LYSO part will be separately discussed.

6.1 Timing Counter Part

The timing counter part of the RDC has 12 plastic scintillator bars and 48 MPPCs for the readout. To increase the acceptance for the scintillation light, several MPPCs are attached on one the scintillator plate. The number of attached MPPCs is two for a 1 cm wide scintillator and three for the 2 cm wide one as can be seen in Fig.6.1.

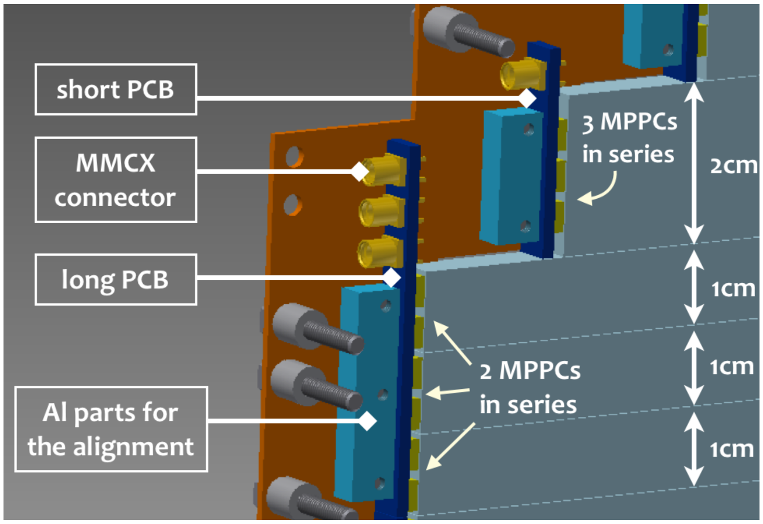

Fig. 6.1: Enlarged figure of Fig.4.12(a). Components are illustrated.

6.1.1 PCB Layout

The Print Circuit Boards (PCBs) are designed to have multi-layers to be compact and to suppress pick-up noise. The signal and ground lines are on different layers. In addition to the two layers, copper layers are set on the both sides for shielding (Fig.6.2). The short and long PCBs are shown in Fig.6.3 and Fig.6.7.

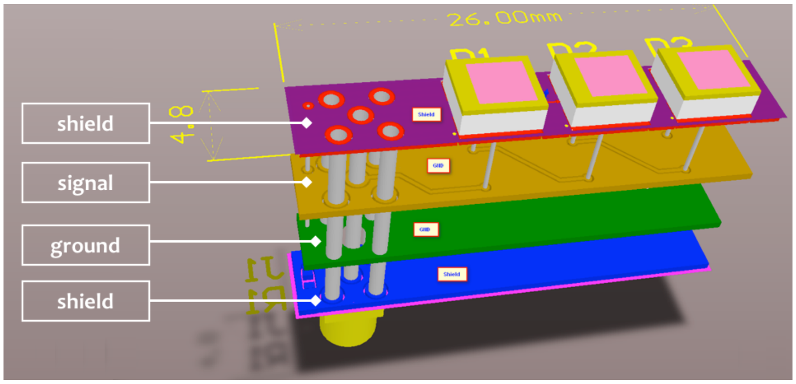

Fig. 6.2: Design of the short PCB

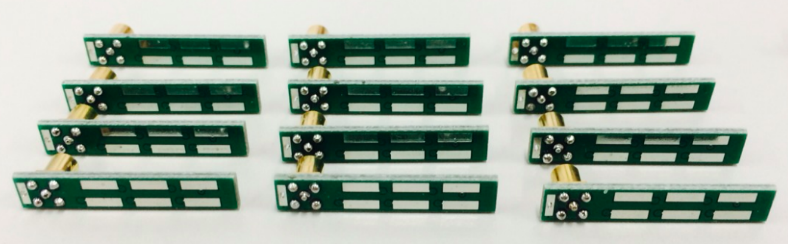

Fig. 6.3: Twelve short PCBs

In our experience, connecting the ground of a MPPC with the chassis ground is effective on reducing noise. In order to avoid slow noise due to ground loops, a capacitor can be inserted between the grounds. The grounding via the capacitor can be used as an option during the experiment depending on the actual noise condition (Fig.6.4, 6.5).

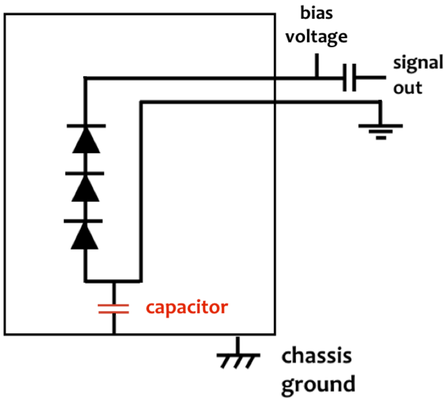

Fig. 6.4: The connection of the chassis ground and the MPPC ground. A capacitor is inserted between them.

Fig. 6.5: A capacitor attached on the PCB

While the short PCB hosts the three MPPCs for one wide scintillator bar, six MPPCs for three narrow scintillators are put on the long PCB because of the space limitation as can be seen in Fig.6.6. In order to avoid the optical crosstalk among the scintillator bars, a light shielding film is inserted between the counters.

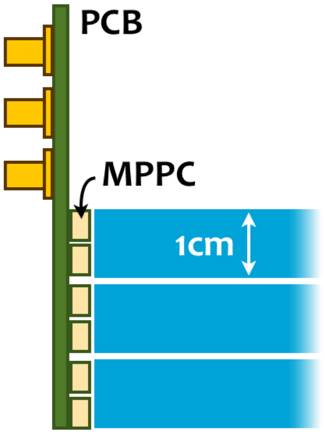

Fig. 6.6: Three scintillation bars with six MPPCs attached to the long PCB

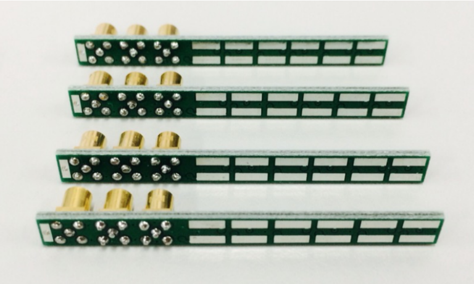

Fig. 6.7: Four long PCBs

6.1.2 Assembly

Some types of SiPMs are known to be damaged by heating. For a safer treatment, the MPPCs are glued on the PCBs with conductive epoxy CW2400 (Fig.6.8), whose properties are given in Table.6.1.

Table 6.1: Properties of CW2400 [24]

Volume Resistivity	<0,001 Ohm-cm
Operation Temperature	-91 to 100 °C
Pot time	8-10 min at 25 °C
Typical thickness	5 mil = 127 μm

Fig. 6.8: Picture of the conductive epoxy CW2400

For the MPPC alignment, polyoxymethylene and acrylic jigs were prepared as shown in Fig.6.9(a) and Fig.6.9(b). The acrylic parts are oil coated to avoid glue adhering (Fig.6.9(c)).

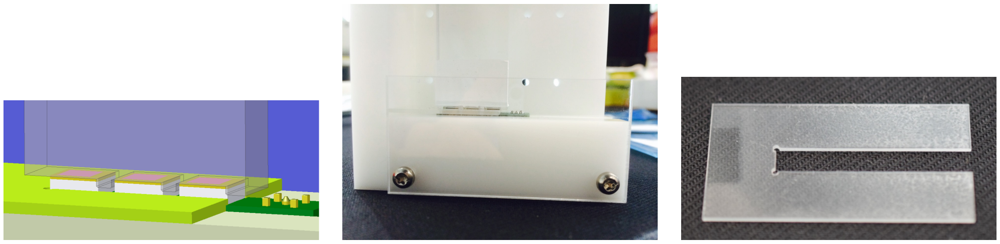

(a) (b) (c)

Fig. 6.9: MPPC alignment jig

MPPCs on the PCB and the plastic scintillators are coupled with optical cement (Fig.6.10). The counter is covered with aluminized mylar as a reflector and a black sheet for light shielding.

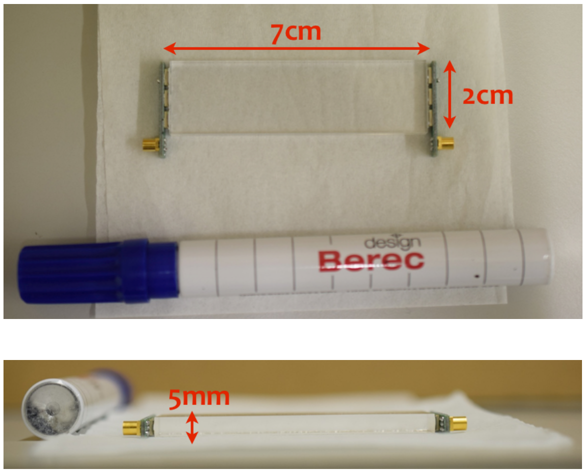

Fig. 6.10: The shortest counter.

6.1.3 Time resolution

The performance for each counter was checked with the following setup: The counter was irradiated by beta-rays from ^{90}Sr and the trigger condition is a hit in a reference counter with time resolution of 30 psec (Fig.6.11). The scintillator size of the reference counter is $5 \times 5 \times 4$ mm^3 and a MPPC is attached for the readout. Here, the time resolution is defined as the sigma of the distribution $\Delta T = (T_0 + T_1)/2 - T_{RC}$ where T_i and T_{RC} are the times measured by the SiPMs attached to the scintillator and by the reference counter respectively (Fig.6.12). All counter showed a time resolution of less than 90 psec which does not include the time resolution of the reference counter.

The position dependence of the time resolution was studied for four counters with different lengths as can be seen in Fig.6.13.

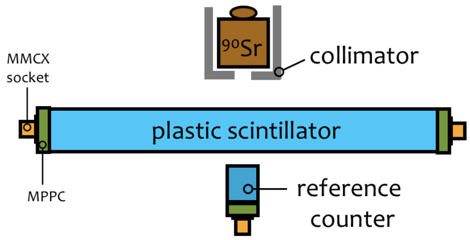

Fig. 6.11: Setup for the performance test of the scintillator bar counters

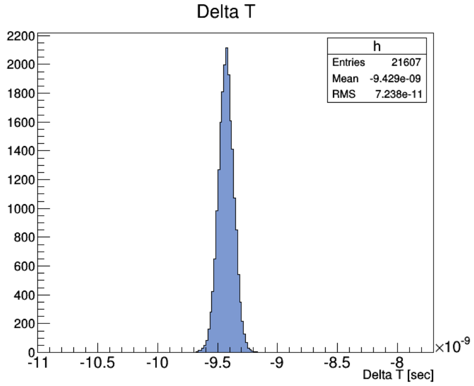

Fig. 6.12: Measured ΔT distribution

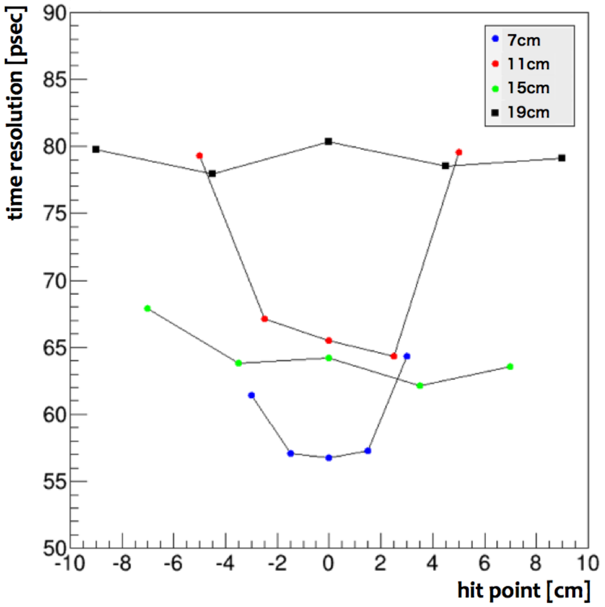

Fig. 6.13: Position dependence of the timing resolution of the scintillator bars

After studying every counter's performance, all of the counters have been assembled in the RDC frame. Each counter has been aligned with small aluminum parts (Fig.6.14).

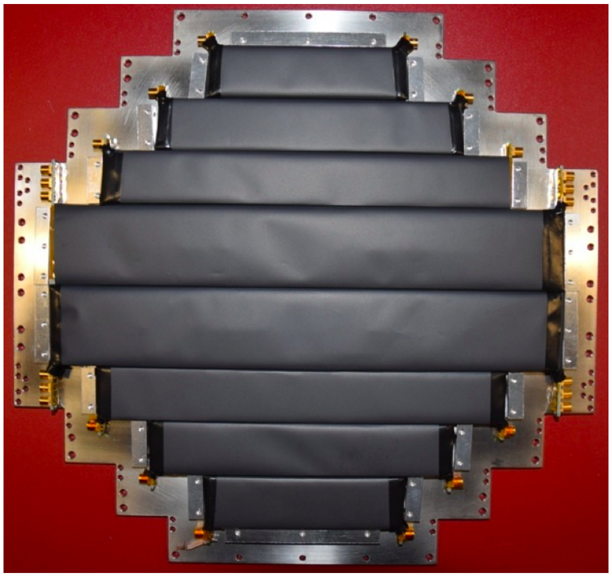

Fig. 6.14: 12 plastic scintillators assembled in the frame.

6.2 Calorimeter Part

The calorimeter part has 76 LYSO crystals and one MPPC is attached to each crystal. While the MPPCs for the plastic scintillators are glued with optical cement, the MPPCs are not glued to the LYSO crystals for ease of maintenance. Instead, the MPPCs are pressed onto the LYSO crystals with non-magnetic springs as can be seen in Fig.6.15. For this purpose, a part of the PCB for the signal transmission is made of a flex-PCB.

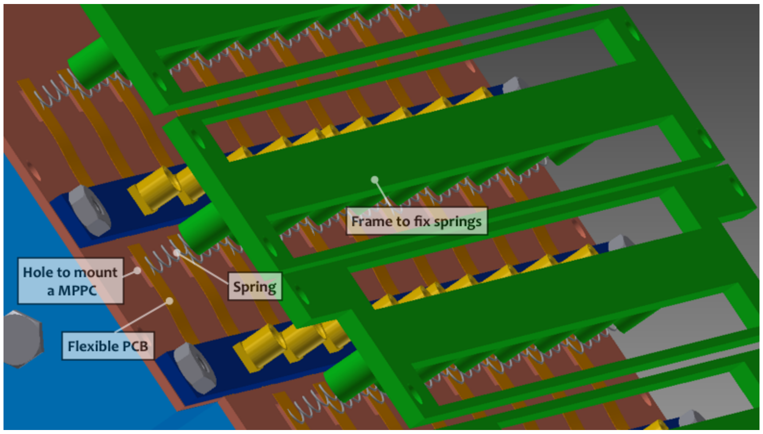

Fig. 6.15: Mechanism to press the MPPCs onto LYSO crystals

6.2.1 PCB Layout

As mentioned above, the PCB for the calorimeter part is partially flexible and the MPPCs attached on the PCB are pressed by springs onto LYSO crystals as can be seen in Fig.6.16 and Fig.6.17.

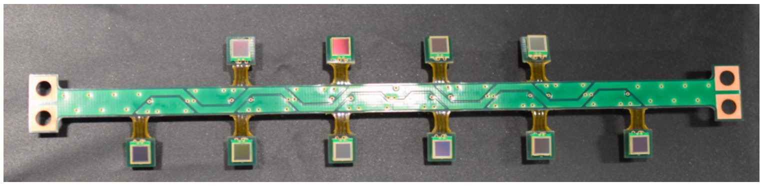

Fig. 6.16: Ten MPPCs soldered on the PCB. The brown branches are flexible parts.

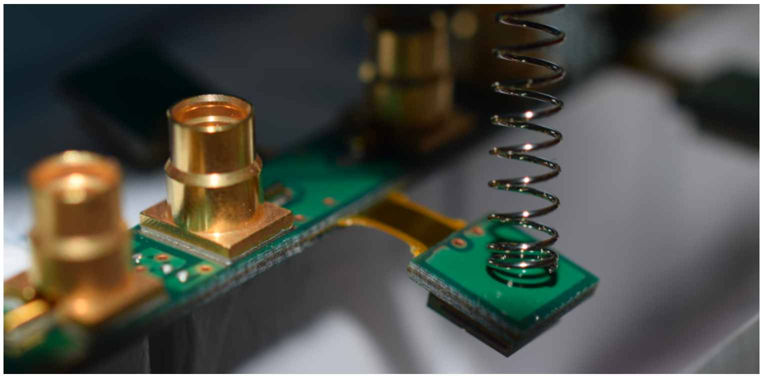

Fig. 6.17: MPPC pressed by a spring

6.2.2 Assembly

The crystals are covered with a 65 μm-thick reflective film which has a window for the coupling with the MPPC.

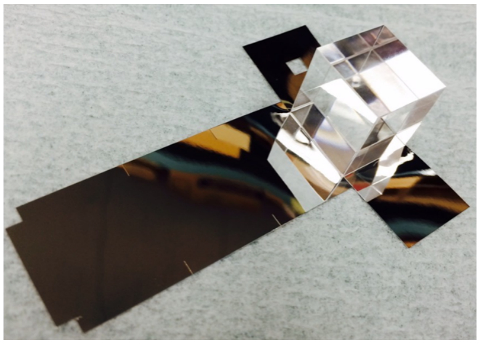

Fig. 6.18: LYSO crystal with a reflective film

Since the LYSO crystals are pushed by the MPPCs with the spring, a support structure is necessary to keep the crystals in position (Fig.6.19). In order to provide enough support while reducing the amount of material, a support plate made of Rohacell and carbon fiber is inserted (Fig.6.20 and Fig.6.21).

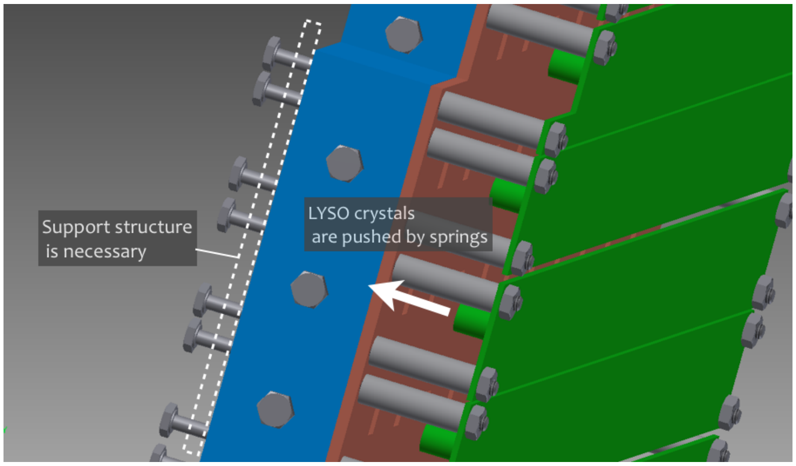

Fig. 6.19: Side view of the LYSO part

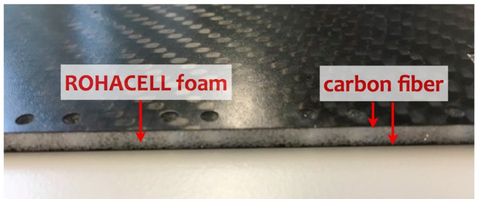

Fig. 6.20: Sandwiched structure made of ROHACELL foam and the carbon fiber layers

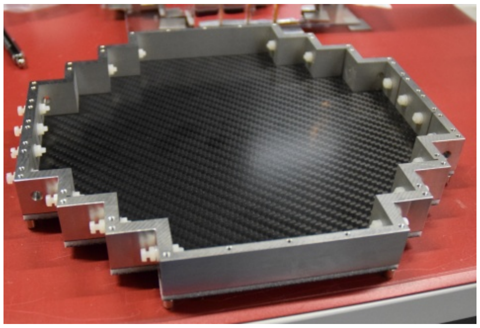

Fig. 6.21: The frame for the LYSO crystals. The white screws attached the side of frame are used for the crystal alignment

All of the LYSO crystals are mounted inside the frame as shown in Fig.6.22. For z-direction alignment of the crystals, a thin Derlin plate is placed between the crystals and the support plate.

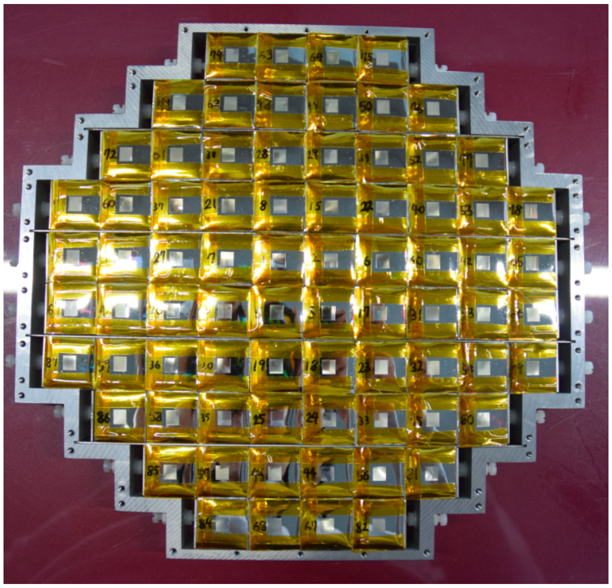

Fig. 6.22: 76 crystals covered with a reflector film and placed in the frame.

On the other side of the crystals, a SUS plate for the support and a Derlin plate for the MPPC alignment are attached (Fig.6.23).

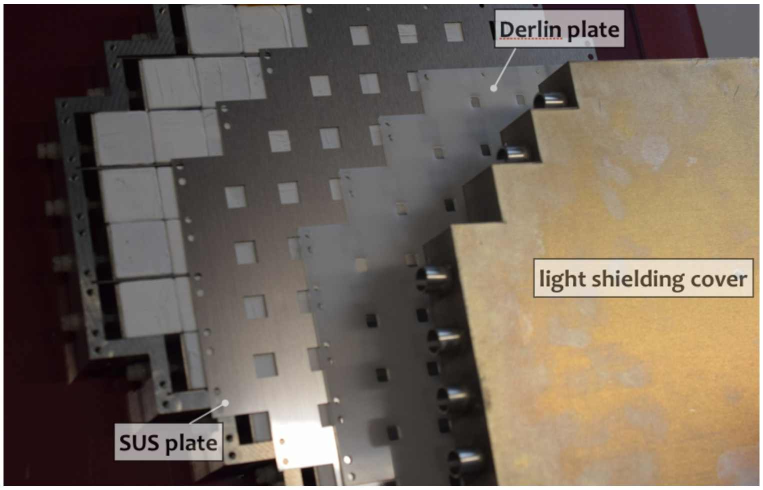

Fig. 6.23: The support and alignment plates. The white blocks in the frame are the dummy crystals for assembly tests

The two plates have 76 windows and the MPPCs can reach the crystals' surface as can be seen in Fig.6.24. Optical grease is used for the coupling.

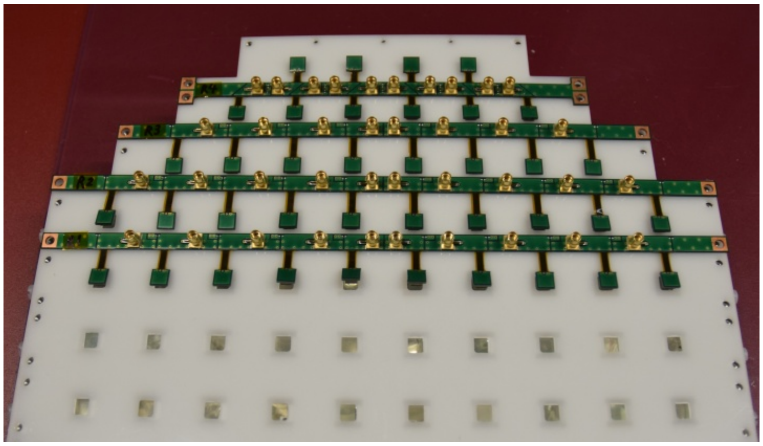

Fig. 6.24: A Derlin plate and four sets of the PCBs with MPPCs. The crystal surface can be seen from the lower windows

The cables from the PCBs are bundled on one side and come out through eight holes in the light-shielding cover. Because of the space limitation for the cabling, some cables are attached on the PCB vertically and are bent by 90 degrees as can be seen in Fig 6.25.

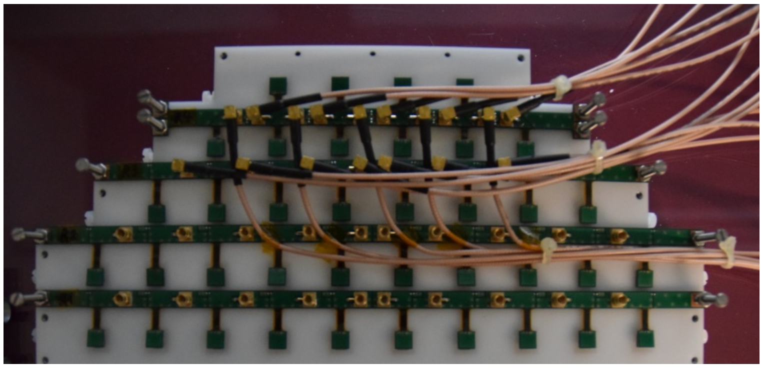

Fig. 6.25: The cabling for calorimeters.

The frame with springs to press the MPPCs is mounted as shown in Fig.6.26. We could observe signals from all channels.

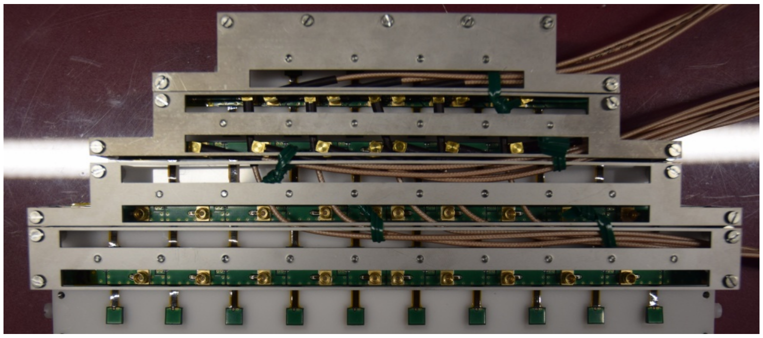

(a) Back view of the MPPCs pushed by springs

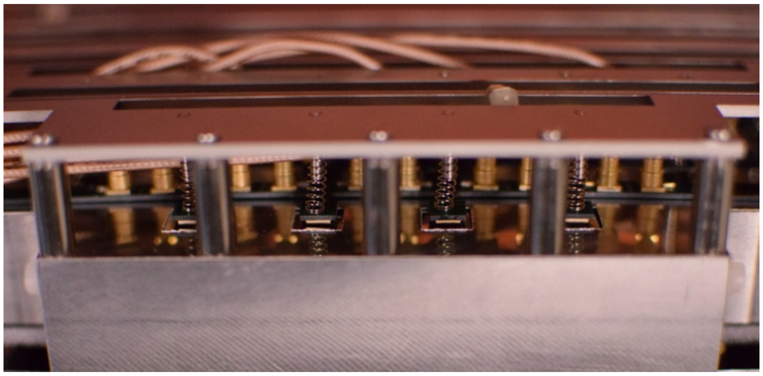

(b) Side view of the MPPCs pushed by springs

Fig. 6.26: The frame and the springs to attach MPPCs on the LYSO crystals

Items to be improved

During the construction, we found that the frame for the RDC downstream is slightly magnetic although it is made of non-magnetic stainless steel. It is said that some types of stainless steel become magnetic during machining. Considering this fact, we will produce a frame made of carbon fiber instead of stainless steel.

Also, some MPPCs did not touch the crystal surface properly. The reflector of the crystals and the polyoxymethylene plate for the MPPC alignment will be improved.

6.3 Installation

The downstream RDC was not installed in the beam area although a mockup of the positron spectrometer and a part of the main positron timing counter were installed and tested in the MEG II detector with a muon beam in the pre-engineering run in 2015. In the downstream COBRA endcap as shown in Fig.6.27, installation of a beam monitoring system and a target monitoring system is also considered in addition to the RDC. Therefore, the downstream RDC installation will be done after defining the installation scheme for all the items.

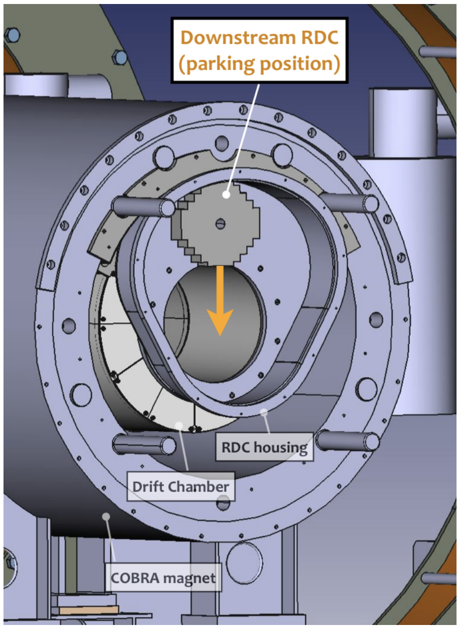

Fig. 6.27: Downstream RDC placed on the edge of the COBRA magnet. The counter in the drawing is set in parking position. The design is preliminary and the details have not been fixed yet.

Chapter 7

Test of the Constructed Detector

The timing counter part and the calorimeter part of the RDC had been separately studied. The next step was checking the compatibility by taking data with the two parts. The two parts were combined and set on the aluminum profiles.

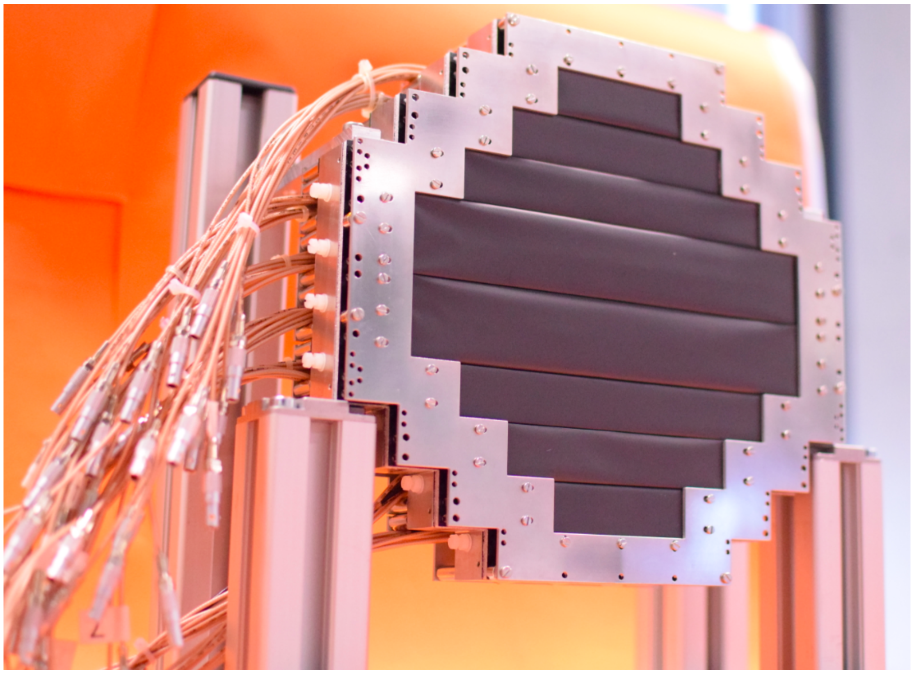

Fig. 7.1: The combined counters

The constructed downstream RDC was tested in the lab with the gamma-ray source Y-88. The goal of the test is to check these items:

- whether all components in the constructed detector work
- the calibration method of each counter

The dominant interaction process of MeV oder gamma-ray in a plastic scintillator was the Compton scattering as shown in Fig.7.2.

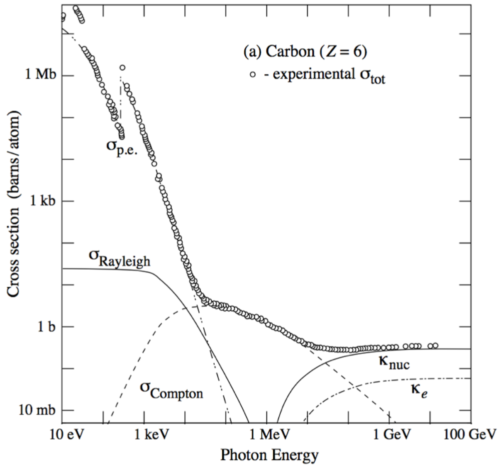

Fig. 7.2: Total cross sections of gamma-rays in carbon [16]. The gamma-rays around 1 MeV mainly interact through the Compton scattering.

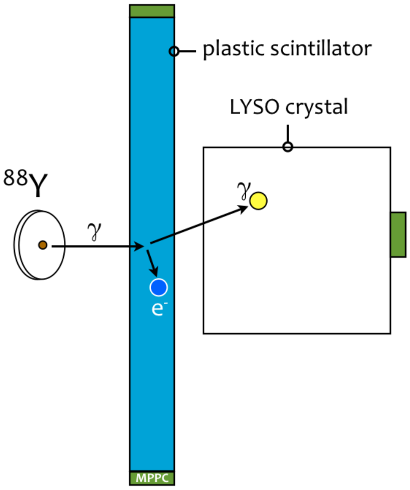

Fig. 7.3: The event where the electron is scattered in the plastic scintillator and the scattered gamma-ray loses all energy in LYSO crystals

Events where the scattered electron is observed in the plastic scintillator and the scattered gamma-ray loses all energy in LYSO crystals as can be seen in Fig.7.3 enables us to reconstruct the incident gamma-ray energy. The constructed counter test uses the total absorption events.

7.1 Simulation

We simulated the energy deposit in the gamma-ray from Y-88 with GEANT4. The gamma-ray source was set at a distance of 1 cm from the center of plastic scintillator.

Since the dominant process of ^{88}Y is the emission of two gamma-rays whose energy are 0.9 MeV and 1.8 MeV as can be seen in Fig.7.4, the gamma-rays with the two energy were produced in each event.

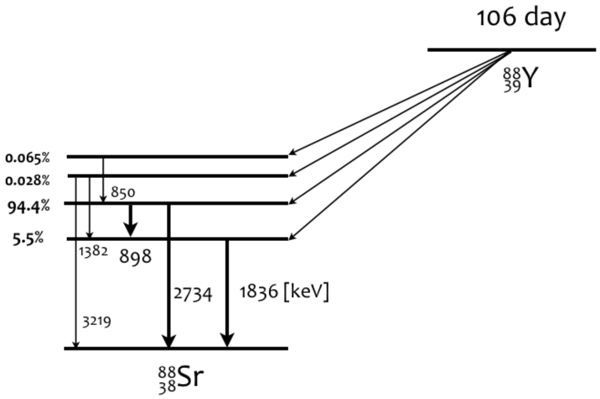

Fig. 7.4: Decay scheme of ^{88}Y

One million events where the gamma-rays enter the plastic scintillator placed in the center were produced. Fig.7.9a shows the RDC detector of the simulation.

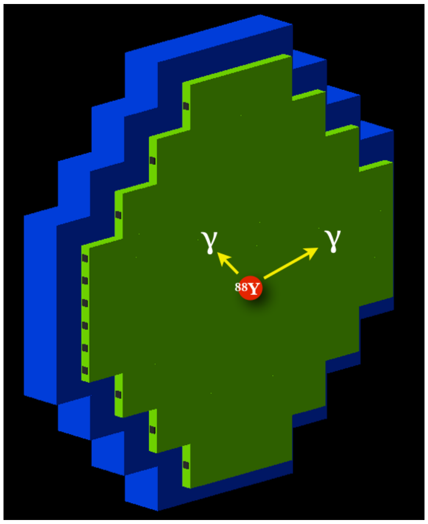

Fig. 7.5: RDC detector of the simulation. The green and blue parts are plastic scintillators and LYSO crystals respectively. The support structure made of ROHACELL and carbon fiber plates is placed between the two parts although it is not drawn. The images of the two gamma-rays emit simultaneously and Y-88 are also drawn.

Fig.7.6 shows the energy deposit in the detectors when a gamma-ray is scattered in the plastic scintillator. It suggests that we are able to see the correlation between the energy deposits in the plastic scintillators and the LYSO crystals.

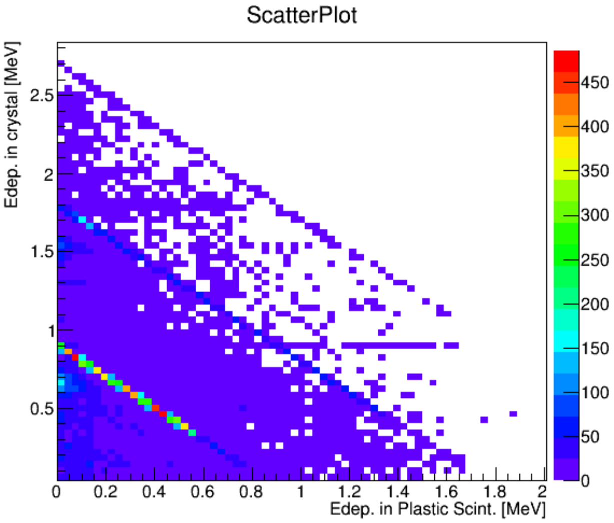

Fig. 7.6: Energy deposit in the crystals vs Energy deposit in the plastic scintillators. The hit in the plastic scintillators is required.

The two horizontal line can be understood as the events where one of the simultaneously emitted gamma-rays scatters off an electron in the plastic scintillator and the other is observed in the crystal, as shown in Fig.7.7.

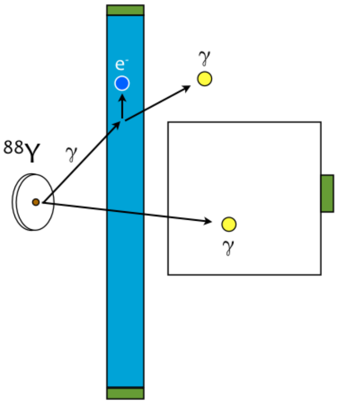

Fig. 7.7: The event where one gamma-ray interacts in the plastic scintillator and the other gamma-ray loses all its energy in the crystal

7.2 Data acquisition

Circuit configuration

The constructed detector was placed in the thermostat chamber and the radioactive source Y-88 was set at a distance of 1 cm from the plastic scintillators as shown in

Fig.7.8. The lead collimator was also placed between the source and the detector. The thickness of the collimator is 1 cm and it has the rectangular hole whose size is 2×1 cm^2.

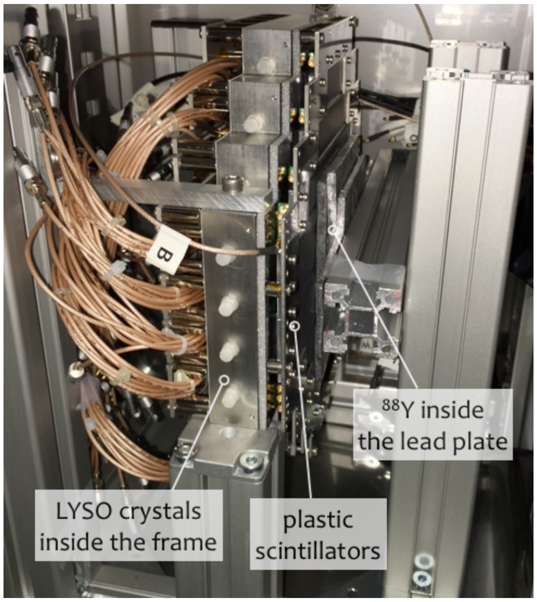

Fig. 7.8: The detector with Y-88 inside the thermostat chamber. The temperature was kept at 30 °C

Because of the limitation of the electronics, one plastic scintillator and nine LYSO crystals were used for the DAQ. In this chapter, ch1 and ch2 is defined as shown in Fig.7.9 (b).

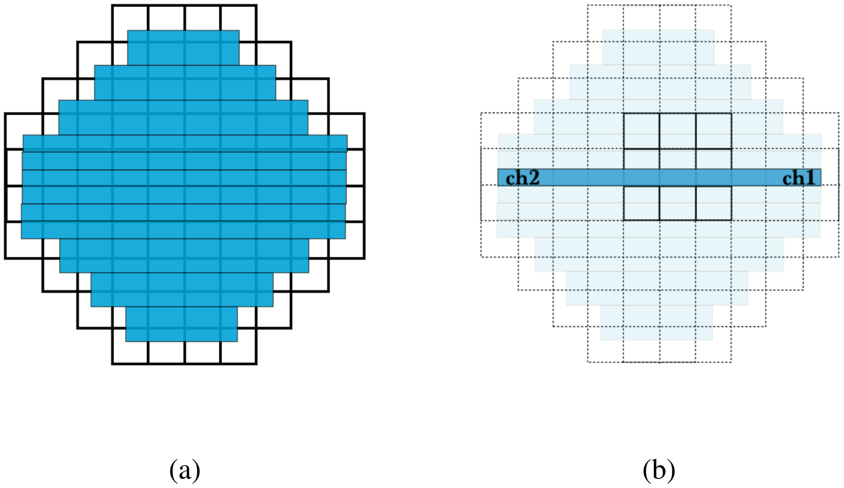

(a) (b)

Fig. 7.9: (a) 76 LYSO and 24 plastic scintillator channels (b) 9 LYSO and 2 plastic scintillator Channels used in the test

The trigger condition is a coincidence between the plastic scintillator and the central crystal. The signals from the plastic scintillator is amplified with an amplifier developed at PSI with a gain of 10. The details of the circuit configuration are illustrated in Fig.7.10, Fig.7.11 and Fig.7.12.

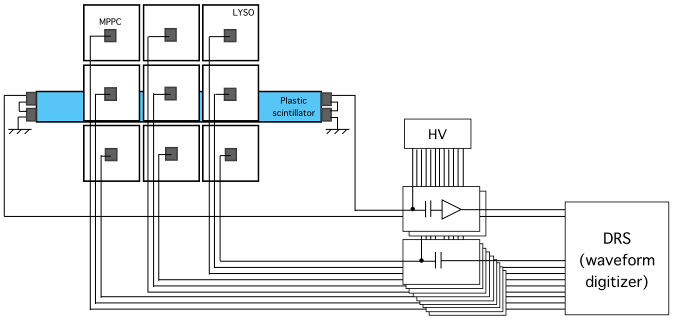

Fig. 7.10: Test setup for measurement of the gamma-ray's total absorption process

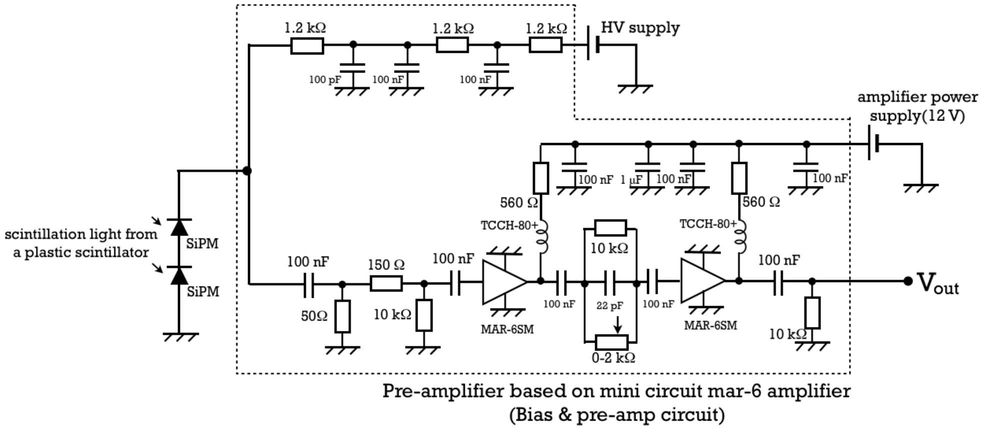

Fig. 7.11: Bias and amplifier circuit diagram applied for the plastic scintillator

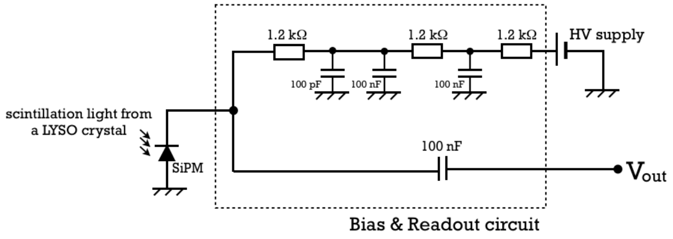

Fig. 7.12: Bias and readout circuit diagram applied for the LYSO crystals

Observed signal

Fig.7.13 shows the typical signal pulses from the plastic scintillator and the LYSO crystal.

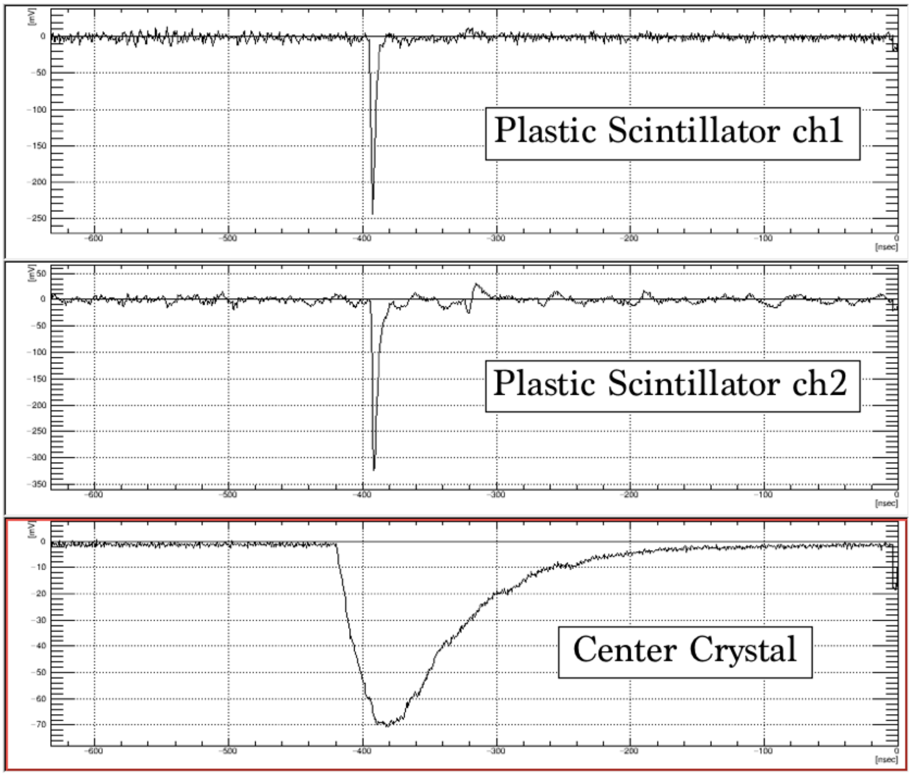

Fig. 7.13: Signal pulses from the plastic scintillator and the central LYSO crystal.

The scatter plot of the pulse heights in the plastic scintillator and in the LYSO crystal is shown in Fig.7.14. In order to minimize the hit position dependence of the pulse height in the plastic scintillator, the geometric mean of the pulse heights of the signals from both ends is used. We can see events with a clear correlation between the signals from the two detectors as expected.

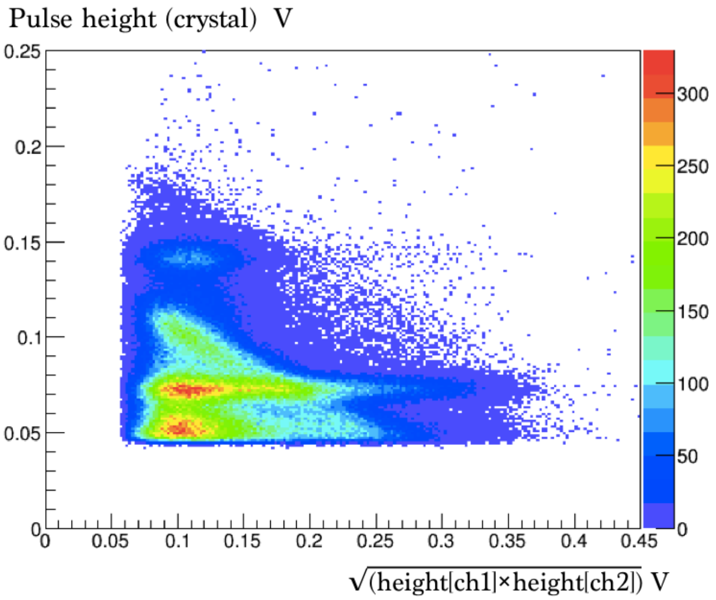

Fig. 7.14: The height in the LYSO crystal vs the height in the plastic scintillator. height[ch1] > 0.05 mV and height[ch2] > 0.05 mV are chosen as the analysis cut.

7.3 Energy Calibration

Plastic scintillator

In the actual MEG II run, the energy scale of the plastic scintillators will be calibrated by using a Landau distribution for Michel positrons passing through the scintillator. We tested the calibration for the scintillator in the lab by using Sr-90. The setup is shown in the Fig.7.15. The source was placed at the same position as for Y-88. The trigger condition is a hit in the reference counter.

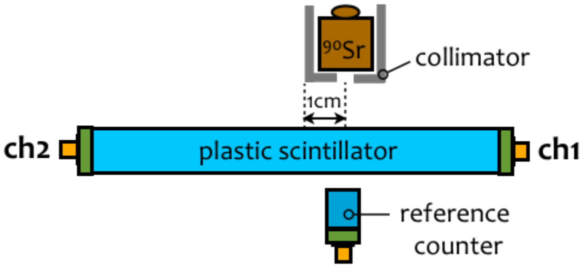

Fig. 7.15: Setup for the energy calibration of the plastic scintillator using Sr-90

Fig.7.16 shows the observed Landau distribution. The energy scale was calibrated by comparing this with the distribution in a simulation (Fig.7.17) where the peak position is 0.9MeV.

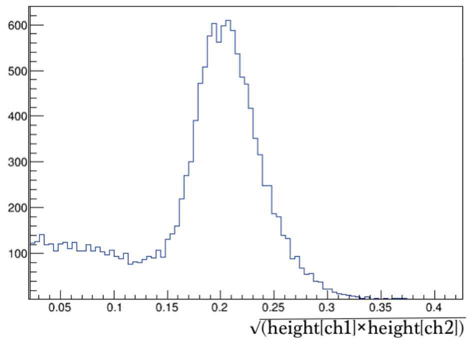

Fig. 7.16: Measured energy deposit of beta-ray in the plastic scintillator

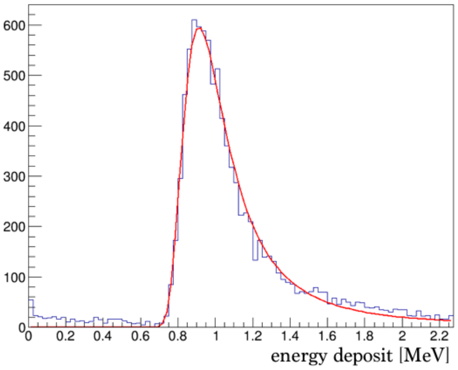

Fig. 7.17: Simulated energy deposit of beta-ray in the plastic scintillator

LYSO crystal

The energy scale for the crystal part can be calibrated with the data of the self-radiation as discussed in section 5.1.3. In addition to the peak of self-radiation, the photo-peaks of 0.9 MeV and 1.8 MeV were also available for the calibration in this test with Y-88 as can be seen in Fig.7.18.

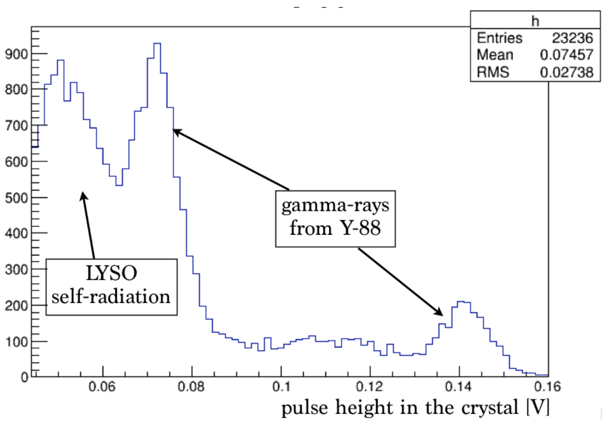

Fig. 7.18: Energy spectrum of the self-radiation and gamma-rays from Y-88

7.4 Result

We selected the events with a correlation between the energy deposits in the two detectors as shown in Fig. 7.19(a). Fig.7.19(b) shows the sum of the energies of the two detectors for the selected events where the peak position is 1.8 MeV as expected.

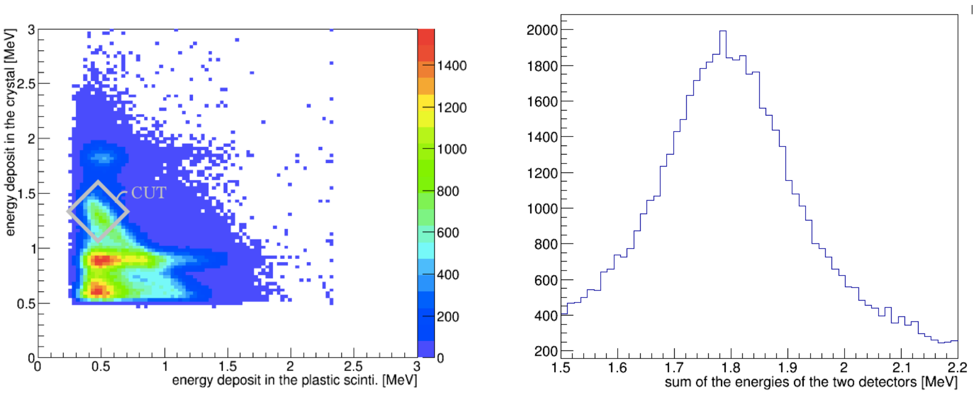

Fig. 7.19: (a) Measured energy deposit in the center LYSO crystals vs one in the plastic scintillator (b) The sum of the energy deposits. The analysis cut: $E_{Cry} + E_{PS} < 2.1 \& E_{Cry} + E_{PS} > 1.6 \& E_{Cry} - E_{PS} < 1.1 \& E_{Cry} - E_{PS} > 0.65$ where E_{Cry} and E_{PS} are the energy deposit in the center LYSO crystal and the plastic scintillator respectively.

Summarizing this chapter, the data with both LYSO crystal and plastic scintillator was successfully taken and the events with a correlation between the energy deposits in the two detectors were observed. We demonstrated that the energy sum between the two detectors worked properly after the calibrations.

Summary and Prospect

Summary

$\mu^+ \to e^+\gamma$ decay has been an important probe to test the new physics and the MEG II experiment to search for the decay aims at starting an engineering runt in 2016. To further improve the sensitivity of the MEG II experiment, the RDC will be newly introduced.

The downstream RDC was approved by the MEG II collaboration and the construction has started. We decided to use LYSO as the calorimeter part and the SiPM for the readout was selected.

The construction has finished and the performances of the timing counter part and the calorimeter part were separately checked in the laboratory. The measured time and energy resolutions were good enough to obtain the sensitivity improvement expected with the RDC.

The constructed detector was tested in the lab. The data with both plastic scintillator and LYSO crystals was successfully taken and the calibration method for each counter worked properly.

The study on the muon beam profile with the upstream RDC is ongoing. The preliminary results suggest that the the effects on the beam profile and rate are small.

Prospect

During the downstream RDC construction, we found some problems in the parts such as the magnetisation of the frame. After solving these problems and checking all of channels, the downstream RDC will be installed in the beam area. We will improve the sensitivity of MEG II using the RDC and try to discover the golden channel, $\mu^+ \to e^+\gamma$.

Acknowledgment

Here, I would like to express my thanks to all of the people who have given me the chance to join the MEG II experiment.

First of all, I would like to express the deepest appreciation for the great support from Prof. Wataru Ootani. Although I faced more difficulties in entering the university than most of the other students, I feel that my effort has paid off because the two years in the Tokyo university and the Paul Scherrer Institute have been the best period of my life.

Second, I thank Prof. Toshinori Mori, the chairperson of the experiment, for letting me join the experiment.

Third, I would like to express my appreciation to the MEG Ⅱ collaborators. Dr. Ryu Sawada, who has proposed the Radiative Decay Counter, supported my research very strongly. Without his persistent help, this thesis would not have been possible. Dr. Yuki Fuji introduced me to the RDC and gave me basic knowledge about research while working together. Dr. Toshiyuki Iwamoto gave me a lot of advice about work in Switzerland. Dr. Yusuke Uchiyama helped my research by giving his incisive comments. Dr. Kei Ieki always comes to the office early and leaves for home late and I have learned a lot from his attitude toward his work. Dr. Malte Hildebrandt and Dr. Peter-Raymond Kettle have kindly taken care of us and gave us a lot of information not only about physics but also about Europe. Dr. Angela Papa have often given us chances to discuss the fiber detector's properties with her group and sometimes we enjoyed lunch or (Italian) coffee together. Dr. Emanuele Ripiccini gave us a lot of opportunities to enjoy our life, such as organizing a weekend party in the guesthouse. I especially would like to express my gratitude to Ms. Giada Rutar who is the best Swiss friend of us Japanese students. I enjoyed the Swiss life with Mr. Daisuke Kaneko, Ms. Miki Nishimura, Mr. Shinji Ogawa, Mr. Kohei Yoshida, Mr. Naoya Shibata, Mr. Mitsutaka Nakao, Mr. Ryoto Iwai, Mr. Souichi Tanaka, Mr. Hiroyuki Nagashima, Mr. Naoyuki Sumi, Mr. Kyohei Noguchi and Ms. Aya Morishita. Especially, always Daisuke made people laugh, Miki made the mood bright, Shinji made things quick, Kohei and Naoya gave us many laughs, Mitsutaka scolded one of his seniors, Ryoto told us many dangerous stories. They gave me many cherished memories.

Fourth, I want to thank the staffs and the secretaries of the International Center for Elementary Particle Physics (ICEPP). In particular I learned many important things, such as how Kansai people should survive in Tokyo, from Mr. MasaHERO Yamatani who will win a nobel prize in the future.

Finally, I would like to express my gratitude to my parents, Masafumi and Mayumi, for their big support.

January 2016
Tokyo
Shota Nakaura

Bibliography

[1] J. Adam et al, New constraint on the existence of the $\mu \rightarrow e\gamma$ decay, May 2013

[2] http://www.united-academics.org/magazine/space-physics/latest-theory-of-everything-to-hit-the-physics-shelves/

[3] The Physics of the Standard Model and Beyond, T. Morii · C. S. Lim · S. N. Mukherjee, World Scientific (2002)

[4] Y. Kuno and Y. Okada, Rev. Mod. Phys. 73, 151 (2001)

[5] S. Antusch, E. Arganda, M.J. Herrero and A.M. Teixeira, J. High Energy Phys. 11 (2006) 090

[6] T. Mori and W. Ootani, Flavour Violating Muon Decays, Progress in Particle and Nuclear Physics,Volume 79, November 2014, Pages 57-94

[7] A. M. Baldini et al, MEG Upgrade Proposal, Feb 2013

[8] AA Grebenuk et al, Search for $\mu^+ \rightarrow e^+\gamma$ down to 10^{-14} branching ratio, May 1999

[9] https://www.psi.ch/bsq/proton-accelerator

[10] T. Doke et al., Jpn. J. Appl. Phys. 41, 1538 (2002).

[11] T. Doke, Portugal Phys. 12, 9 (1981).

[12] K. Fujii et al, High-accuracy measurement of the emission spectrum of liquid xenon in the vacuum ultraviolet region, Nuclear Instruments and Methods in Physics Research Section A: Accelerators, Spectrometers, Detectors and Associated Equipment, Volume 795, 21 Sep 2015

[13] Stefan Ritt et al, Application of the DRS Chip for Fast Waveform Digitizing, Nucl. Instr. Meth. A 623, 486-488 (2010)

[14] Stefan Ritt, DRS4 Evaluation Board User ’ s Manual, 2014

[15] SGC BC418-420-422 Data Sheet, BC-418, BC-420, BC-422 Premium Plastic Scintillators

[16] W.-M. Yao, *et al.* [Particle Data Group], Journal of Physics G **33**, 1 (2006).

[17] Charles Kittel, *Introduction to Solid State Physics*, John Wiley & Sons, 2004.

[18] http://pdg.lbl.gov/2015/listings/rpp2015-list-muon.pdf

[19] M.L.Brooks et al, Phys. Rev. Lett. 83 (1999) 1521.

[20] Saint-Gobain PreLudeTM 420 data sheet

[21] J. Rosado et at, "Modeling crosstalk and afterpulsing in silicon photomultipliers", arXiv:1409.4564

[22] Hamamatsu Photonics, MPPC data sheet.

[23] Hamamatsu Photonics, MPPC data sheet S13360 series.

[24] CHEMITRONICS Technical Data Sheet CircuitWorks Conductive Epoxy TDS #CW2400

[25] W.Ootani, Silicon Photomultiplier (SiPM) Status and Perspectives, Special Workshop on Photon Detection with MPGDs, June 2015 CERN

[26] http://advansid.com/resources/the-silicon-photmultiplier

[27] Y. Uchiyama, “Analysis of the First MEG Physics Data to Search for the Decay $\mu^+ \to e^+\gamma$”, Ph. D. Thesis, the University of Tokyo (2009)

[28] Y. Nishimura, “ A Search for the Decay $\mu^+ \to e^+\gamma$ Using a High-Resolution Liquid Xenon Gamma-Ray Detector ” Ph. D. Thesis, the University of Tokyo (2010)

[29] H. Nishiguchi, “ An Innovative Positron Spectrometer to Search for the Lepton Flavour Violating Muon Decay with a Sensitivity of 10^{-13} ” , Ph. D. Thesis, the University of Tokyo (2008)

[30] R. Sawada, “A Liquid Xenon Scintillation Detector to Search for the Lepton Flavour Violating Muon Decay with a Sensitivity of 10^{-13} ” , Ph. D. Thesis, the University of Tokyo (2005)

[31] Y. Fuji "Search for the Lepton Flavor Violating Muon Decay $\mu+ \to$ e+ γ with a Sensitivity below 10-12 in the MEG Experiment ” , Ph. D. Thesis, the University of Tokyo (2013)